The Auger spectrum of benzene

Nayanthara K. Jayadev[a], Anthuan Ferino-Pérez[b],
Florian Matz[b], Anna I. Krylov[a], and Thomas-C. Jagau[b]
[a] Department of Chemistry, University of Southern
California, Los Angeles, CA 90089, United States of America
[b] Department of Chemistry, KU Leuven, B-3001 Leuven, Belgium

We present an *ab initio* computational study of the Auger electron spectrum of benzene. Auger electron spectroscopy exploits the Auger-Meitner effect and, although it is established as an analytic technique, the theoretical modeling of molecular Auger spectra from first principles remains challenging. Here, we use coupled-cluster and equation-of-motion coupled-cluster theory combined with two approaches to describe the decaying nature of core-ionized states: (i) Feshbach-Fano resonance theory and (ii) the method of complex basis functions. The spectra computed with these two approaches are in excellent agreement with each other and also agree well with experimental Auger spectra of benzene. The Auger spectrum of benzene features two well-resolved peaks at Auger electron energies above 260 eV that correspond to final states with two electrons removed from the $1e_{1g}$ and $3e_{2g}$ highest occupied molecular orbitals. At lower Auger electron energies, the spectrum is less well resolved and the peaks comprise multiple final states of the benzene dication. In line with theoretical considerations, singlet decay channels contribute more to the total Auger intensity than the corresponding triplet decay channels.

I. INTRODUCTION

X-ray spectroscopies are widely used for probing the electronic structure of molecules and materials[1–3]. Based on transitions involving core electrons, they exploit special features of the core orbitals—their localized nature, the element specificity of their energies, and the sensitivity to the environment of these energies[1–7]. Progress in experimental techniques such as laser technology and, more specifically, the higher quality of X-ray beams, has motivated recent efforts to advance theoretical capabilities for modeling core-level transitions.[5,8,9]

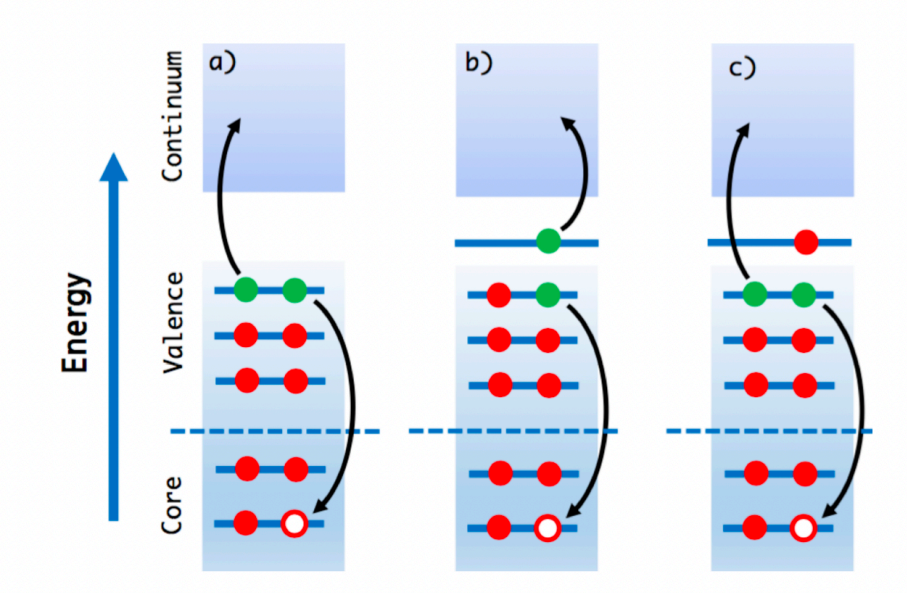

FIG. 1: Different types of Auger decay: (a) regular Auger decay, (b) resonant participator decay, and (c) resonant spectator decay. *Reproduced with permission from Ref. 14.*

Irradiation with X-rays creates vacancies in core orbitals, producing highly excited or ionized states. Alternatively, core-hole states can also be created by nuclear transformations such as electron capture or internal conversion of some radionuclides. In molecules with light atoms—C, N, and O—which are most relevant to organic chemistry, core-hole states relax predominantly via autoionization processes collectively referred to as the Auger-Meitner effect[10,11]. In non-radiative Auger decay, a valence electron fills the core vacancy, liberating sufficient energy to eject another electron, called the Auger electron, into the continuum. Different types of this process are shown in Fig. 1: core-ionized states, produced, for example, in X-ray photoionization spectroscopy (XPS), undergo regular Auger decay, whereas core-excited states, produced in X-ray absorption spectroscopy (XAS), undergo resonant participator or spectator Auger decay. Less common are double and triple Auger decay in which two or three electrons are simultaneously emitted, resulting in multiply charged cations.[12,13]

In Auger electron spectroscopy,[15] the intensity of the emitted Auger electrons is recorded as a function of their kinetic energy. Auger electron spectroscopy benefits from the element- and environment-sensitivity of core orbitals and, therefore, can provide information about the electronic structure not accessible by other techniques[1]. It has been employed to

characterize with high accuracy and high spatial resolution the chemical composition of surfaces[16–19], materials[20–22], nanostructures[23,24], and gas-phase molecules[25–28].

Auger electrons find uses beyond spectroscopy, e.g., in radiotherapy and precision medicine.[29–32] Because Auger decay produces multiple electron tracks in the vicinity of the emission site, typically within 500 nm, it can deposit large amounts of energy into the surrounding molecules. This ability of Auger emitters to deliver considerable levels of radiation to a specific target[33–35] has motivated the therapeutic use of molecules labeled with radionuclides that emit Auger electrons upon nuclear decay.

Theoretical modeling of Auger processes is difficult owing to the metastable nature of core-ionized and core-excited states, which are embedded in the ionization continuum. Conventional quantum chemistry methods are formulated for discrete bound states with L^2-integrable wavefunctions and thus cannot describe states subject to electronic decay. One can circumvent this problem by artificial stabilization of core-hole states by means of the core-valence separation[36] (CVS). This approach, in which decaying states are approximated as bound states, delivers excellent energies in most cases. However, energies alone are not sufficient for modeling Auger spectra, because a complete description requires decay widths as well.

In this contribution, we compute decay widths for the core-ionized states of benzene and construct its Auger spectrum. As a prototypical aromatic molecule, benzene is often used as a model system to test new spectroscopic techniques[37–42] and benchmark theoretical methods[43–50]. The high symmetry and multiple core orbitals make Auger decay in benzene particularly interesting, which motivated several experimental and theoretical studies.[51–57]

In the early experiment by Spohr *et al.*, Auger electrons were generated by electron impact[51], which likely produces highly excited molecules, giving rise to an Auger spectrum containing regular and resonant contributions. Later, Köppe and co-authors used X-ray radiation to produce core-ionized states[52]; they reported an Auger spectrum of benzene obtained with 390 eV radiation, which they referred to as the sudden limit, as well as an Auger spectrum obtained using lower excitation energies closer to XAS transitions. It is expected that the former spectrum should be dominated by non-resonant Auger decay whereas the latter spectrum should feature resonant contributions. The most recent experiment by Carniato *et al.* employed higher energy radiation (510 eV) and measured Auger electrons in coincidence with photoelectrons in order to eliminate the resonant contributions to the

spectrum.[53]

Fig. 2 shows the Auger spectra of benzene from the three experiments. The spectra have similar shape, but show noticeable differences both in the peak positions and the intensities. The position of the lowest peak (labeled L in Fig. 2) differs by 0.58 eV and even more troubling is the fact that it is not possible to align the positions of all major peaks by a constant shift. For example, if the spectra are aligned by the lowest peak then the position of the highest peak (labeled H in Fig. 2) varies by 1.44 eV, an so on. This is illustrated in Figs. **??**, **??**, and **??** in the Supplemental Information (SI).

Theoretically, Auger decay in benzene was studied by Tarantelli *et al.* using a statistical approach, which assumes that all decay channels have identical partial widths.[55] Specifically, they computed the decay channels, i.e., the dicationic states of benzene, with second-order algebraic diagrammatic construction (ADC(2))[58,59] and constructed the spectrum using the density of states as a proxy of the intensities. On the basis of these calculations, Tarantelli *et al.* were able to interpret the main features in the Auger spectrum.[55]

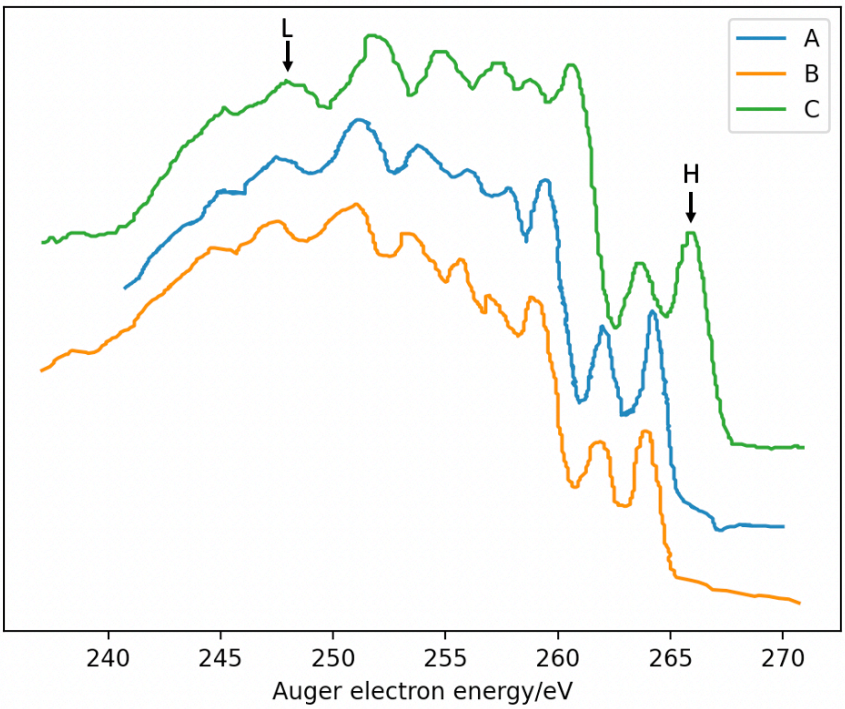

FIG. 2: Auger spectrum of benzene from (a) Spohr *et al.*,[51] (b) Rennie *et al.*,[52] and (c) Carniato *et al.*[53]

In view of the challenges faced by quantitative experimental measurements of Auger

spectra and the noticeable discrepancies between the three experimental Auger spectra of benzene, there is a need for accurate theoretical modeling. By using a high-level description of the electronic structure and computing the Auger decay widths explicitly, we hope to clarify the nature of the main spectral features in the Auger spectrum of benzene and to provide a benchmark for future experiments.

We use two different theoretical approaches to compute the decay widths of the core-ionized states: Feshbach-Fano resonance theory[60–62] and the method of complex basis functions (CBF),[63] which is based on complex scaling.[64,65] The comparison between these different theoretical approaches, and between theory and experiment, provides insights into the Auger spectrum of benzene and into Auger decay in general.

Both approaches originate from non-Hermitian quantum mechanics, which offers a powerful and elegant framework for treating molecular electronic resonances.[66–70] The Schrödinger equation is reformulated such that the resonances are separated from the continuum and become isolated states with L^2-integrable wavefunctions and complex energies,

$$E_{\mathrm{res}} = E - i\frac{\Gamma}{2}, \tag{1}$$

where the real part E describes the energy of a resonance and the imaginary part gives its decay width Γ, which is inversely proportional to the lifetime. The Feshbach-Fano approach and the method of complex basis functions represent two techniques to achieve such reformulation in practice.[67–70]

These ideas were recently exploited to model molecular Auger decay rates in the framework of coupled-cluster (CC) theory[71] and its equation-of-motion (EOM) extensions:[72–74] Skomorowski and Krylov have developed a method based on the Feshbach-Fano formalism[14,75] whereas Matz and Jagau have developed methods based on CBFs.[76,77]

The structure of the paper is as follows: Sec. II outlines the details of our theoretical modeling, Sec. III presents the numerical results, and Sec. IV offers concluding remarks.

II. THEORETICAL AND COMPUTATIONAL DETAILS

A. Relevant electronic states of benzene

Fig. 3 shows the occupied molecular orbitals (MOs) of benzene and their irreducible representations. The electronic configuration of the ground state of neutral benzene is

$$\mathrm{X}^1\mathrm{A}_{1g} = (\mathrm{core})^{12}(2a_{1g})^2(2e_{1u})^4(2e_{2g})^4(3a_{1g})^2(2b_{1u})^2(1b_{2u})^2(3e_{1u})^4(1a_{2u})^2(3e_{2g})^4(1e_{1g})^4 \ , \quad (2)$$

where the core comprises six doubly occupied orbitals

$$(\mathrm{core})^{12} = (1a_{1g})^2(1e_{1u})^4(1e_{2g})^4(1b_{1u})^2 \ . \quad (3)$$

Following Wentzel,[80,81] we treat Auger decay as a two-step process in which the second step, filling of the core hole and ejection of the Auger electron, is independent of the first step, creation of the core vacancy. Thus, our theoretical treatment focuses on the second step. Fig. 4 shows a sketch of the electronic states relevant for our modeling: the neutral ground state, the core-ionized states, which are the initial states in the Auger process, and the doubly ionized valence states, which represent the final states. The core-ionized states are metastable and decay producing free electrons and doubly ionized valence states. Different doubly ionized states correspond to different decay channels, giving rise to Auger electrons with specific energies. The rates of decay into the respective doubly ionized target states determine the intensities in the Auger spectrum: Faster decay rates correspond to a higher probability of decay into the respective doubly ionized target state.

Given that the four core-ionization energies (IEs) of benzene differ by only 0.1 eV, we assume that any of the six core orbitals can be ionized, i.e., all six core-ionized states ($^2\mathrm{A}_{1g}$, $^2\mathrm{E}_{1u}$, $^2\mathrm{E}_{2g}$, $^2\mathrm{B}_{1u}$) contribute equally to the total Auger spectrum. A rough estimate of the number of possible Auger transitions is $6 \times 15 \times 15 = 1,350$ because the core vacancy can be filled by an electron taken from any valence shell and the Auger electron can also originate from any valence shell. In this estimate, we do not take into account degenerate shells and the spin multiplicity of the doubly ionized target states. Also, we do not include channels resulting from three-electron processes, i.e., those leading to 3-hole-1-particle ($3h1p$) target states of the dication because these channels are expected to have lower intensity. Furthermore, we do not consider resonant Auger decay and focus on the non-resonant Auger

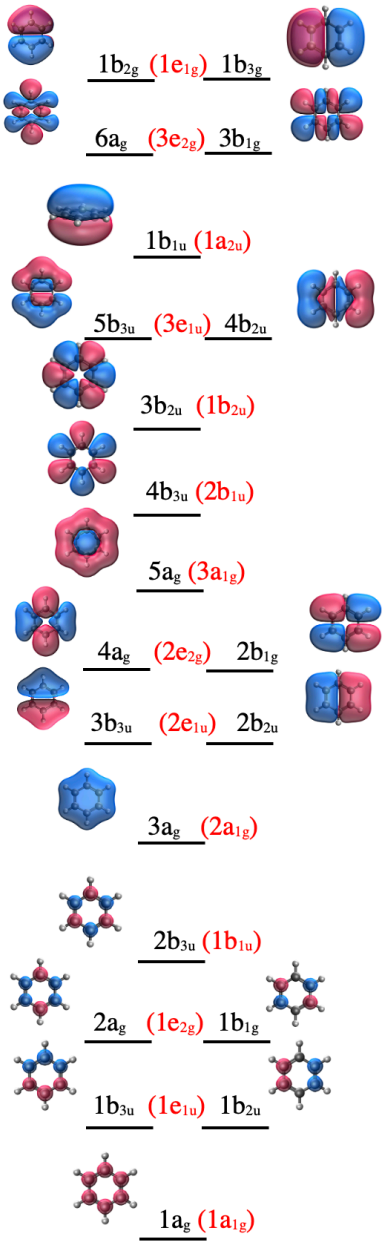

FIG. 3: Occupied molecular orbitals of benzene. Irreducible representations are given for the D_{6h} point group (in red) using Mulliken convention[78] and for the largest Abelian subgroup (D_{2h}, in black), using Q-Chem's symmetry notation.[79]

decay. This is justified by the setup of the most recent measurement, which supposedly excludes contributions from resonant Auger decay.[53]

Using a one-electron picture and Koopmans' theorem, the energies of the Auger electrons

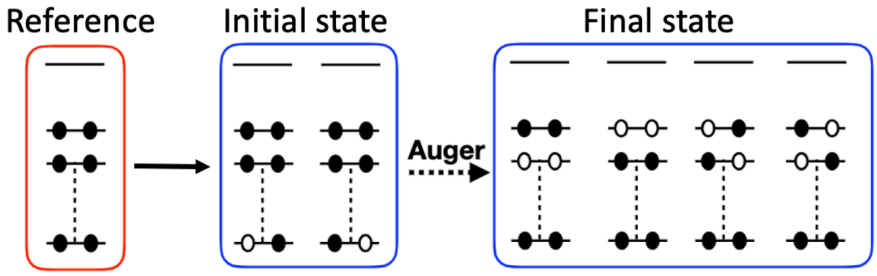

FIG. 4: Initial and final states in regular Auger decay.

are:[82]

$$E_{\text{Auger}} = \epsilon_{v1} + \epsilon_{v2} - \epsilon_{\text{core}}, \tag{4}$$

where ϵ_{v1} and ϵ_{v2} are the energies of the valence holes created by the Auger decay and ϵ_{core} is the energy of the core orbital with the hole. In correlated treatments, different $2h$ configurations can mix, giving rise to correlated doubly ionized states, which we call DIP states. The positions of the peaks in the Auger spectrum are then

$$E_{\text{Auger}} = E_{\text{DIP}} - E_{\text{coreIP}}. \tag{5}$$

Further, correlated treatments are able distinguish singlet and triplet Auger channels. As per Fig. 3, the highest-energy Auger electrons should correspond to the DIP states with 2 holes in the $1e_{1g}$ highest occupied molecular orbital (HOMO) of benzene.

Because the IEs of the core orbitals are very close (ca. 0.1 eV), one can anticipate that the positions of the peaks in the Auger spectrum of benzene follow the energies of the DIP states and that the intensity pattern follows the density of DIP states. Indeed, this approach has been used in earlier theoretical treatments of the Auger spectrum of benzene.[55] Although the density of correlated DIP states can provide a zero-order picture of the Auger spectrum, a quantitative treatment needs to account for different probabilities associated with different decay channels.[81–83] These probabilities are proportional to the partial widths of the metastable core-ionized states for decay into a particular channel. If all decay channels are considered, these partial widths sum up to Γ from Eq. (1). In the following two sections—II B and II C—we discuss and compare our two approaches for computing these partial widths, i.e., Feshbach-Fano resonance theory and the method of complex basis functions. We show that accounting for partial widths leads to significant

changes in the Auger intensities as compared to an estimate based on the density of DIP states.

We note that the contributions of triplet decay channels are expected to be smaller than the contributions of singlet channels.[82,84] The dominance of singlet channels is also confirmed by experiments on atoms, where the peaks in the Auger spectrum can be unambiguously mapped onto the decay channels.[85] In the Appendix we analyze the contributions of singlet and triplet channels for the two many-body approaches used in this work.

Specific details of theoretical protocols are given below. All calculations were carried out using the Q-Chem package.[86,87]

B. Feshbach-Fano approach

For the Feshbach-Fano calculations, we employ CC and EOM-CC theory with single and double substitutions (CCSD and EOM-CCSD, respectively)[72–74,88] and its extensions to core-level states using CVS.[43,89–97] The reference state in these calculations corresponds to neutral benzene and is treated by CCSD:

$$|\Psi^{\mathrm{CC}}\rangle = e^{T}|\Phi_0\rangle \ , \tag{6}$$

$$T = T_1 + T_2 = \sum_{ia} t_i^a \, a^\dagger i + \frac{1}{4}\sum_{ijab} t_{ij}^{ab} \, a^\dagger b^\dagger j i, \tag{7}$$

where $|\Phi_0\rangle$ is the Hartree-Fock reference determinant, which defines the separation between occupied and virtual orbital spaces. Following the standard notation, indices $i, j, k, \ldots$ denote orbitals from the occupied space, indices $a, b, c, \ldots$ denote orbitals from the virtual space, and indices $p, q, r, \ldots$ denote orbitals that can be either occupied or virtual.

The core-hole states are described by EOM-IP-CCSD as

$$|\Psi^{\mathrm{IP}}\rangle = R^{\mathrm{IP}} e^{T}|\Phi_0\rangle \ , \tag{8}$$

$$R^{\mathrm{IP}} = R_1^{\mathrm{IP}} + R_2^{\mathrm{IP}} = \sum_{i} r_i \, i + \frac{1}{2}\sum_{ija} r_{ij}^{a} \, a^\dagger j i, \tag{9}$$

and the EOM-IP amplitudes r_i and r_{ij}^a are found by diagonalizing the similarity transformed Hamiltonian, $\bar{H} = e^{-T} H e^{T}$ in the space of $1h$ and $2h1p$ determinants. The IEs are directly obtained as eigenvalues of the EOM-IP-CCSD equations. We use the CVS scheme where the EOM-IP operators R_1^{IP} and R_2^{IP} are restricted to operators that include at least one core

orbital.[89–92] This makes the core-ionized states artificially bound and separates them from the double ionization continuum. The doubly ionized target states are described by the DIP variant of EOM-CCSD:[98–100]

$$|\Psi^{\rm DIP}\rangle = R^{\rm DIP} e^T |\Phi_0\rangle \ , \tag{10}$$

$$R^{\rm DIP} = R_1^{\rm DIP} + R_2^{\rm DIP} = \frac{1}{2}\sum_{ij} r_{ij}\, ij + \frac{1}{6}\sum_{ijka} r^a_{ijk}\, a^\dagger kji \ , \tag{11}$$

and the EOM-DIP amplitudes r_{ij} and r^a_{ijk} are determined by diagonalization of $\bar{H}$ in the space of $2h$ and $3h1p$ determinants.

In the Feshbach-Fano approach, a resonance state is obtained as the result of the interaction between a bound discrete state and continuum states.[60–62] The Feshbach projection operators Q and P divide the full Hilbert space into bound and continuum subspaces, respectively,[61] and these subspaces are coupled via the matrix elements of the many-body Hamiltonian between the bound and continuum configurations. By using the Löwdin partitioning technique,[62] the problem of computing the resonance energy is formulated as an eigenproblem of a non-Hermitian effective Hamiltonian $\mathcal{H}_{QQ}$ defined in the Q-space:

$$\mathcal{H}_{QQ}\,|\tilde{\Psi}\rangle = \tilde{\mathcal{E}}\,|\tilde{\Psi}\rangle \ , \tag{12}$$

$$\tilde{\mathcal{E}} = \mathcal{E} - i\frac{\Gamma}{2} \ , \tag{13}$$

$$\mathcal{H}_{QQ} = H_{QQ} + H_{QP}\, G_P^{(+)}(E)\, H_{PQ} \ , \tag{14}$$

$$G_P^{(+)}(E) = \lim_{\epsilon\to 0} \frac{1}{E + i\epsilon - H_{PP}} \ . \tag{15}$$

In practice, Eqs. (12)–(15) are solved perturbatively. In zeroth order, one computes the eigenstates $|\Psi\rangle$ of the bound-space Hamiltonian H_{QQ}. Then, the complex resonance energy $\tilde{\mathcal{E}}$ is computed using the first-order correction, i.e., by computing a matrix element between the bound and continuum states

$$\tilde{\mathcal{E}} \approx E + E^{(1)} = E + \langle \Psi \,|\, H_{QP}\, G_P^{(+)}\, H_{PQ} \,|\, \Psi\rangle, \tag{16}$$

giving rise to

$$\mathcal{E} = {\rm Re}\langle\Psi|\mathcal{H}_{QQ}|\Psi\rangle \approx E + \sum_\mu P.V. \int_0^\infty dE' \, \frac{\langle\Psi|H_{QP}|\chi^\pm_{\mu,E'}\rangle\langle\chi^\pm_{\mu,E'}|H_{PQ}|\Psi\rangle}{E - E_\mu - E'} \ , \tag{17}$$

$$\Gamma = -2\,{\rm Im}\langle\Psi|\mathcal{H}_{QQ}|\Psi\rangle \approx \sum_\mu 2\pi\, \langle\Psi|H_{QP}|\chi^\pm_{\mu,E-E_\mu}\rangle\langle\chi^\pm_{\mu,E-E_\mu}|H_{PQ}|\Psi\rangle = \sum_\mu \Gamma_\mu \ . \tag{18}$$

Here, μ denotes the decay channels and E_μ the associated threshold energies, while $\chi^{\pm}_{\mu,E}$ refers to scattering states, which are normalized according to $\langle \chi^{\pm}_{\mu,E} | \chi^{\pm}_{\mu',E'} \rangle = \delta_{\mu\mu'}\,\delta(E-E')$.

The Feshbach-Fano approach has recently been applied by Skomorowski and Krylov to compute Auger decay rates using EOM-CC wave functions.[14] In their approach, CVS was used to define the projector Q. The bound part of a resonance state, that is, Ψ from Eqs. (17) and (18), can be computed by CVS-EOM-IP-CCSD and the continuum states $\chi^{\pm}_{\mu,E}$ are represented by products of EOM-DIP-CCSD states and free-electron states.

In this approach, the final expression for the partial width corresponding to the decay of an initial core-hole state into channel μ is

$$\Gamma_\mu = 2\pi g_\alpha \int d\Omega_{\mathbf{k}} \left(\sum_p h^\mu_{p\mathbf{k}} \gamma^p + \frac{1}{2} \sum_{pqr} \langle pq||\mathbf{k}r\rangle^\mu \, \Gamma^{pq}_r \right) \left(\sum_p h^\mu_{\mathbf{k}p} \gamma_p + \frac{1}{2} \sum_{pqr} \langle \mathbf{k}r||pq\rangle^\mu \, \Gamma^r_{pq} \right) \,, \tag{19}$$

where g_α accounts for spin degeneracy and $\Omega_{\mathbf{k}}$ for the angle of the emitted electron with momentum $\mathbf{k}$. $h_{p\mathbf{k}}$ and $\langle pq||\mathbf{k}r\rangle^\mu$ are matrix elements of the one-electron and two-electron parts of the Hamiltonian.

Because of the two-electron nature of Auger decay, the dominant contribution to Eq. (19) comes from the two-body Dyson orbitals Γ^{pq}_r and Γ^r_{pq},[83] which connect EOM-IP-CCSD (Ψ^{N-1}) and EOM-DIP-CCSD (Ψ^{N-2}) states

$$\Gamma^p_{qr} = \langle \Psi^{N-2} | p^\dagger q r | \Psi^{N-1} \rangle \tag{20}$$

$$\Gamma^{pq}_r = \langle \Psi^{N-1} | p^\dagger q^\dagger r | \Psi^{N-2} \rangle \,. \tag{21}$$

These are contracted with two-electron integrals in which index $\mathbf{k}$ corresponds to a continuum orbital,

$$\langle \Psi^{N-2} | a_{\mathbf{k}} O_2 | \Psi^{N-1} \rangle = \frac{1}{2} \sum_{pqr} \langle \mathbf{k}r||pq\rangle \Gamma^r_{pq}, \tag{22}$$

$$\langle \Psi^{N-1} | O_2 a^\dagger_{\mathbf{k}} | \Psi^{N-2} \rangle = \frac{1}{2} \sum_{pqr} \langle pq||\mathbf{k}r\rangle \Gamma^{pq}_r \,. \tag{23}$$

Here, $a^\dagger_{\mathbf{k}}$ denotes the creation operator corresponding to a free electron with momentum $\mathbf{k}$ and O_2 is the two-electron part of the Hamiltonian.[81,83] Because the EOM-CC Hamiltonian is not symmetric, both left and right Dyson orbitals, i.e., Γ^{pq}_r and γ^p as well as Γ^r_{pq} and γ_p, need to be computed.

In this work, we describe the continuum orbital $\mathbf{k}$ by plane waves. Complete expressions and details of the calculations of mixed Gaussian-plane-wave integrals are available in Ref.

14. The integration over $\Omega_{\mathbf{k}}$ is carried out using Lebedev's quadrature and we found that for benzene a very fine integration grid of order 17 is needed for converged results; calculations with the default grid of order 5 yield partial widths that break symmetry-imposed constraints. Sample inputs are given in the SI.

The structure of benzene was optimized with RI-MP2/cc-pVTZ; the respective Cartesian coordinates are given in the SI. The fully uncontracted 6-311(2+,+)G** basis set was used in the CVS-EOM-IP-CCSD and EOM-DIP-CCSD calculations[45,101] to evaluate the partial widths according to Eq. (19). In line with the frozen-core (fc) CVS approach, the core electrons, that is, the K-shells on carbons, were frozen in all valence calculations.[91] The decay widths were convoluted with a Gaussian function with a fixed full width at half maximum equal to 1.15 eV. The so-obtained Auger intensities were then combined with the Auger electron energies calculated according to Eq. (5) to generate the final Auger spectra. In addition, natural orbitals (NOs) were computed to analyze the many-body wave functions in terms of a molecular orbital framework.[102,103]

C. Complex basis function approach

In the CBF method, we describe the metastable core-ionized states directly by CCSD, without invoking CVS. In these calculations, $|\Phi_0\rangle$ from Eqs. (6) and (7) is a determinant with a core hole. To obtain the required high-energy solutions of the unrestricted Hartree-Fock (UHF) equations, the MOM (maximum orbital overlap) algorithm is used.[104,105] The IEs are then computed as differences between the total CCSD energies of the core-ionized states and that of the neutral molecule, hence the name ΔCCSD.

In the CBF method,[63,106,107] the description of Auger decay is based on an L^2-representation of the resonance wave function obtained through analytical continuation of the Hamiltonian to the complex plane. A particular advantage of this approach is that no assumption needs to be made about the functional form of the wave function of the Auger electron. The complex resonance energy from Eq. (1) is computed as eigenvalue of a non-Hermitian Hamiltonian without invoking perturbation theory and the total decay width is obtained as $\Gamma = -2\,\mathrm{Im}(E_{\mathrm{res}})$.

The CBF method is related to complex scaling of the Hamiltonian[64,68] through the iden-

tity

$$E_{\mathrm{res}} = \frac{\langle\Psi(r)|\hat{H}(re^{i\theta})|\Psi(r)\rangle}{\langle\Psi(r)|\Psi(r)\rangle} = \frac{\langle\Psi(re^{-i\theta})|\hat{H}(r)|\Psi(re^{-i\theta})\rangle}{\langle\Psi(re^{-i\theta})|\Psi(re^{-i\theta})\rangle} \tag{24}$$

with θ ($0 < \theta < \pi/4$) as the complex-scaling angle. In the CBF method, the complex-scaled wave function on the right-hand side of Eq. (24) is expressed in terms of Gaussian functions with a scaled exponent that take the form

$$\chi_\mu(r, A) = N_\mu(\theta)\, S_\mu(r_A)\, \exp\bigl[-\alpha\, e^{-2i\theta} r_A^2\bigr], \tag{25}$$

where N_μ is a normalization constant and S_μ is a polynomial that depends on the angular quantum number of χ_μ. By scaling only selected basis functions, one obtains a finite-basis representation of the exterior complex-scaled Hamiltonian of Eq. (24).[108,109] In contrast to complex scaling of the Hamiltonian, the CBF method is compatible with the Born–Oppenheimer approximation and thus applicable not only to atoms but also to molecular electronic resonances.

While the resonance energy E_{res} is independent of the scaling angle θ in the complete basis set limit, a dependence does exist when working with a finite basis. We determine the optimal value for θ through minimization of $|d(E_{\mathrm{res}} - E_0)/d\theta|$, where E_0 is the energy of neutral benzene in the present case. While $\mathrm{Im}(E_0)$ would be zero in the complete basis set because the ground state of benzene is stable against loss of electrons, this is not the case in a finite basis. Previous applications have shown that minimizing this energy difference generally leads to better results than minimizing $|dE_{\mathrm{res}}/d\theta|$.[76,110–112] Further theoretical details of the CBF method can be found elsewhere.[63,70,111,113]

We note that a variety of applications have shown that CBFs combined with CC theory provide an accurate description not only of Auger decay but of other types of electronic resonances such as temporary anions and molecules in static electric fields as well.[111–114]

To compute partial Auger decay widths in the framework of the CBF approach, Matz and Jagau developed two different procedures.[76,77] The first one can be viewed as a generalization of CVS[36]. In this procedure, partial widths are evaluated by applying projectors that are specific to a particular Auger decay channel.[77] The approach works well combined with CCSD, EOM-CCSD, and configuration interaction singles (CIS) wave functions but has the disadvantage that each decay channel requires a separate calculation.

The second approach is based on the decomposition of the imaginary energy and works only for CCSD wave functions.[76] This approach, which has the advantage that all partial

widths can be evaluated from a single calculation, was used in the present work. The partial width of a particular decay channel is computed as the contribution to the imaginary part of the CCSD energy

$$E_{\mathrm{CCSD}} = E_{\mathrm{HF}} + \sum_{ijab} \Big(\frac{1}{4} t_{ij}^{ab} + \frac{1}{2} t_i^a t_j^b\Big) \langle ij||ab\rangle \tag{26}$$

from those amplitudes t_{ij}^{ab} where a or b refers to the core hole and i and j are the occupied valence orbitals that are empty in the target state. Note that, because of the two-electron nature of Auger decay, the Hartree–Fock energy would be real-valued in the complete basis set limit and the non-zero value of $\mathrm{Im}(E_{\mathrm{HF}})$ results from using a finite basis.

In the CBF approach, where partial decay widths are evaluated using Eq. (26) alone, there seemingly is no need to compute the wave functions of the doubly ionized target states. However, the energies of these target states are needed to construct the Auger spectrum. In a first approximation, we used Eq. (4) and the orbital energies obtained in the Hartree–Fock calculations on the core-ionized states for this purpose. However, Eq. (4) is a rather crude approximation of the Auger electron energy and Eq. (5) represents a natural improvement.

In contrast to the Feshbach-Fano approach based on EOM-CC wave functions, there is no obvious way to evaluate Eq. (5) in the framework of the CBF approach based on CCSD wave functions for the core-ionized states. In the present work, we evaluated Eq. (5) in the same way as in Sec. II B, that is, as differences between EOM-DIP-CCSD and EOM-IP-CCSD energies. However, we found that the assignment of the partial widths computed with CCSD using Eq. (26) to channel energies computed with EOM-DIP-CCSD is not straightforward. This is because the EOM-DIP-CCSD eigenvectors R^{DIP} often are not represented by a single transition but have contributions from several orbitals. We constructed the partial width for each DIP state by summing up those CCSD partial widths whose involved orbitals i and j correspond to the leading EOM-DIP-CCSD amplitudes ($r_{ij} > 0.1$). We then weighted the contributions by the corresponding DIP amplitudes r_{ij} and linearly combined the resulting widths for the DIP states with leading amplitudes corresponding to the same transition. We only considered DIP states with dominant $2h$ character, because $3h1p$ configurations do not contribute to the Auger decay process.

The structure of benzene was taken from Ref. 76. This structure differs from the one used in Sec. II B on the order of 0.001 Å, which is irrelevant for our purposes. All calculations were carried out using a modified cc-pCVTZ basis set where s- and p-shells were replaced by

those from cc-pCV5Z. In the CBF-CCSD calculations, three complex-scaled *s*-, *p*-, and *d*-shells were added to all C atoms. The resulting basis set is denoted cc-pCVTZ(5sp)+3(*spd*) and is provided in the SI.

The optimal complex-scaling angle θ_{opt} was determined as 12° by minimization of $|d(E_{\text{res}}-E_0)/d\theta|$. For this purpose, the CBF-CCSD energies of neutral benzene and of the core-ionized $^2\text{A}_{1g}$ state were recalculated in the range $6° - 16°$ in steps of 1°. The same optimal value for θ was assumed for the other core-ionized states since there is evidence that θ_{opt} varies little between resonances with similar electronic structures.[70]

Benzene has four distinct core-ionized states, two of which are doubly degenerate. When starting from reference determinants with a core hole, six core-ionized states can be constructed because the degeneracy of the $^2\text{E}_{1u}$ and $^2\text{E}_{2g}$ states is artificially lifted. Accordingly, we computed six sets of partial widths corresponding to the six core-ionized states. The effect of this artificial symmetry breaking on the results is discussed in Sec. III. The final Auger spectra were built by applying a Gaussian broadening function with a full width at half maximum equal to 1.15 eV to all decay widths in complete analogy to Sec. II B.

III. RESULTS AND DISCUSSION

A. Energies of core-ionized and valence doubly ionized states

Table I shows the IEs of benzene. As anticipated, they are very close, spanning the energy range from 290.78 eV to 290.86 eV at the CVS-EOM-IP-CCSD/u6-311(2+,+)G** level. The computed IEs agree well with the experimentally determined core-ionization threshold for benzene of 290.42 eV.[52] Using the larger cc-pCVTZ(5sp) basis improves the agreement by about 0.1 eV. The comparison of the different theoretical methods reveals that CBF-EOM-IP-CCSD yields energies that are systematically too high by about 1.5 eV. CBF-ΔCCSD yields energies that are even higher by ca. 1 eV, which can be explained by a better description of core relaxation in this approach.The last column of Table I shows that the degeneracy of the $^2\text{E}_{1u}$ and $^2\text{E}_{2g}$ states is lifted in the ΔCCSD calculations. This artificial splitting amounts to about 1 eV.

In the simulation of the Auger spectrum using the Feshbach-Fano approach we computed 143 EOM-DIP-CCSD states (73 singlets and 70 triplets) with dominant $2h$ character,

TABLE I: Core ionization energies (in eV) of benzene.

		CVS-EOM-IP-CCSD	CVS-EOM-IP-CCSD	CBF-EOM-IP-CCSD	CBF-ΔCCSD
State[a]	Core orbital[b]	u6-311(2+,+)G**[c]	cc-pCVTZ(5sp)[c]	cc-pCVTZ(5sp) +3(*spd*)[c]	cc-pCVTZ(5sp) +3(*spd*)[c]
$^2A_{1g}$	$1a_g$	290.86	290.74	292.04	293.10
$^2E_{1u}$	$1b_{3u}$	290.85	290.72	292.02	291.82
$^2E_{1u}$	$1b_{2u}$	290.85	290.72	292.02	292.81
$^2E_{2g}$	$2a_g$	290.80	290.68	291.98	291.82
$^2E_{2g}$	$1b_{1g}$	290.80	290.68	291.98	292.77
$^2B_{1u}$	$2b_{3u}$	290.78	290.66	291.96	293.03

[a]Irreducible representations are given for the full molecular point group, D_{6h}, using Mulliken convention.
[b]Irreducible representations are given for the computational point group, D_{2h}, using Q-Chem convention.
[c]For the definition of basis sets, see Secs. II B and II C. CBF calculations were performed with a scaling angle of 12°.

whereas in the simulation using the CBF approach we computed 166 EOM-DIP-CCSD states (88 singlets and 78 triplets). These states span the range from 24 eV to 43 eV, which corresponds to Auger electrons with energies of 244–267 eV. In both simulations, the number of computed target states is less than the estimated total number of $2h$ configurations because of configuration mixing, which stabilizes some states while destabilizing others. The destabilized states appear at much higher energies and mix with $3h1p$ configurations, which reduces their contributions to the Auger spectrum. Our calculations do not include decay channels corresponding to Auger electrons with energies below 244 eV.

Table II shows the energies and the character of the 14 lowest DIP states. The basic structure of the double ionization spectrum is consistent with Koopmans' theorem, i.e., the energies of the orbitals involved in the ionization process. Our DIP energies and the character of the corresponding wave functions also agree well with the ADC(2) results from Ref. 55. In accordance with well-known trends for excitation energies, ADC(2) yields double ionization energies that are consistently lower than EOM-DIP-CCSD energies by 1.5–2.0 eV.

In agreement with Hund's rules, the ground state of doubly ionized benzene is a triplet

TABLE II: Double ionization energies (eV) of the 14 lowest doubly ionized states of benzene. The composition of the wave functions in terms of the leading DIP amplitudes is also given.

State	Energy[a]	Energy[b]	Energy[c]	Composition[a]
$^3A_{2g}$	24.85	25.17	23.34	$1e_{1g}^{-2}$ (0.67)
$^1E_{2g}$	25.48	25.80	23.96	$1e_{1g}^{-2}$ (0.66)
$^1A_{1g}$	25.92	26.25	24.59	$1e_{1g}^{-2}$ (0.64), $1a_{2u}^{-2}$ (0.28)
$^3B_{1g}$	27.85	28.14	26.19	$3e_{2g}^{-1}1e_{1g}^{-1}$ (0.47)
$^3E_{1u}$	27.90	28.26	26.07	$1e_{1g}^{-1}1a_{2u}^{-1}$ (0.67)
$^3E_{1g}$	27.96	28.24	26.30	$3e_{2g}^{-1}1e_{1g}^{-1}$ (0.47)
$^1B_{1g}$	28.05	28.33	26.44	$3e_{2g}^{-1}1e_{1g}^{-1}$ (0.46), $1a_{2u}^{-1}1b_{2u}^{-1}$ (0.11)
$^3B_{2g}$	28.07	28.35	26.41	$3e_{2g}^{-1}1e_{1g}^{-1}$ (0.47)
$^1E_{1g}$	28.16	28.43	26.55	$3e_{2g}^{-1}1e_{1g}^{-1}$ (0.46), $1a_{2u}^{-1}3e_{1u}^{-1}$ (0.11)
$^1B_{2g}$	28.25	28.52	26.63	$3e_{2g}^{-1}1e_{1g}^{-1}$ (0.47)
$^1A_{1u}$	29.90	30.16	28.08	$1e_{1g}^{-1}3e_{1u}^{-1}$ (0.47)
$^3E_{2u}$	29.98	30.26	28.32	$1e_{1g}^{-1}3e_{1u}^{-1}$ (0.41), $3e_{2g}^{-1}1a_{2u}^{-1}$ (0.11), $1e_{1g}^{-1}1b_{2u}^{-1}$ (0.11)
$^3A_{1u}$	30.04	30.29	28.22	$1e_{1g}^{-1}3e_{1u}^{-1}$ (0.47)
$^1E_{2u}$	30.04	30.31	28.39	$1e_{1g}^{-1}3e_{1u}^{-1}$ (0.37), $3e_{2g}^{-1}1a_{2u}^{-1}$ (0.38), $1e_{1g}^{-1}1b_{2u}^{-1}$ (0.15)

[a]Computed with EOM-DIP-CCSD/u6-311(2+,+)G**.
[b]Computed with EOM-DIP-CCSD/cc-pCVTZ(5*sp*).
[c]Computed with ADC(2), taken from Tarantelli *et al.*[55]

($^3A_{2g}$), which is described as ionization from the doubly degenerate HOMO ($1e_{1g}$). According to EOM-DIP-CCSD calculations, its double-ionization energy is 24.85 eV, which is close to the experimentally determined value of 24.65 eV.[115] The two singlet states, which also result from ionization of the HOMO ($^1E_{2g}$ and $^1A_{1g}$), appear just 0.6 eV and 1.1 eV above the ground state.

Above these three states, there is a gap of almost 2 eV, followed by a cluster of seven states, which span a range of 0.4 eV from 27.85 eV to 28.25 eV. Six of them are ionizations from HOMO and HOMO-1 ($1e_{1g} \otimes 3e_{2g} = {}^{1/3}E_{1g} \oplus {}^{1/3}B_{1g} \oplus {}^{1/3}B_{2g}$), whereas the last one is a triplet state ($^3E_{1u}$) corresponding to ionization of HOMO and HOMO-2 ($1e_{1g} \otimes 1a_{2u}$). Interestingly, the corresponding singlet state ($^1E_{1u}$) is 3 eV higher in energy while the

singlet-triplet splittings of the states described as HOMO $\otimes$ HOMO-1 amount to at most 0.2 eV. This difference arises due to the very different values of the respective exchange integrals, $\langle 1e_{1g}\,1e_{1g}\,|\,1a_{2u}\,1a_{2u}\rangle \approx 0.341$ hartree, $\langle 1e_{1g}\,1e_{1g}\,|\,3e_{2g}\,3e_{2g}\rangle \approx 0.036$ hartree, which were computed by summing over all degenerate orbitals.

Next comes a second distinct gap of 1.7 eV after which the structure of the DIP spectrum becomes less resolved. The next group of doubly ionized states, which is only partly included in Table II, results from ionization from HOMO and HOMO-3 but these states are separated by only 1 eV from higher-lying ones. Notably, the lowest-lying state in this group is a singlet ($^1\mathrm{A}_{1u}$) and not a triplet. This can be explained by the low value of the exchange integral $\langle 1e_{1g}\,1e_{1g}\,|\,3e_{1u}\,3e_{1u}\rangle \approx 0.067$ hartree.

As one can see from Table II, the low-lying DIP states are well represented by a single $2h$ configuration. However, this changes at higher energies, where we observe considerable configuration mixing so that many states cannot be described by a single $2h$ configuration. This has also been observed in the ADC(2) study of doubly ionized benzene by Tarantelli *et al.*[55] and in an ADC(2) study of doubly-ionized fluorinated benzenes.[57] We note that some of the higher-lying DIP states also show considerable $3h1p$ character. While the energy of these satellite states is overestimated by EOM-DIP-CCSD, the effect on the Auger spectrum is small because of their small contribution to the two-body Dyson orbital (Eqs. (20) and (21)).

The analysis of the EOM-DIP-CCSD wave functions in terms of natural orbitals (NOs) and their populations shown in Fig. 5 confirms these observations. For the neutral ground state, the shape of the NOs is very similar to that of the canonical HF MOs from Fig. 3. By comparing the NO occupations of the DIP states with those of the neutral reference state, one can infer the character of the orbitals from which the electrons are removed in the course of Auger decay. For example, for the $^3\mathrm{A}_{2g}$ state at 24.85 eV and the $^1\mathrm{A}_{1g}$ state at 25.92 eV, the occupation numbers of the $1b_{3g}$ and $1b_{2g}$ NOs change from 1.92 to 1.01 relative to the neutral reference. This implies that a total of 1.82 electrons are removed from these NOs, which together represent the $1e_{1g}$ shell in the full point group, while 0.18 electrons are removed from other orbitals. For the $^3\mathrm{B}_{1g}$ state at 27.85 eV, the occupation numbers of the $6a_g$ and $1b_{3g}$ NOs change from 1.95 to 1.53 and those of the $3b_{2g}$ and $1b_{2g}$ NOs from 1.92 to 1.50. This means that the a total of 1.68 electrons are removed from the $1e_{1g}$ and $3e_{2g}$ shells and 0.32 electrons are removed from other orbitals.

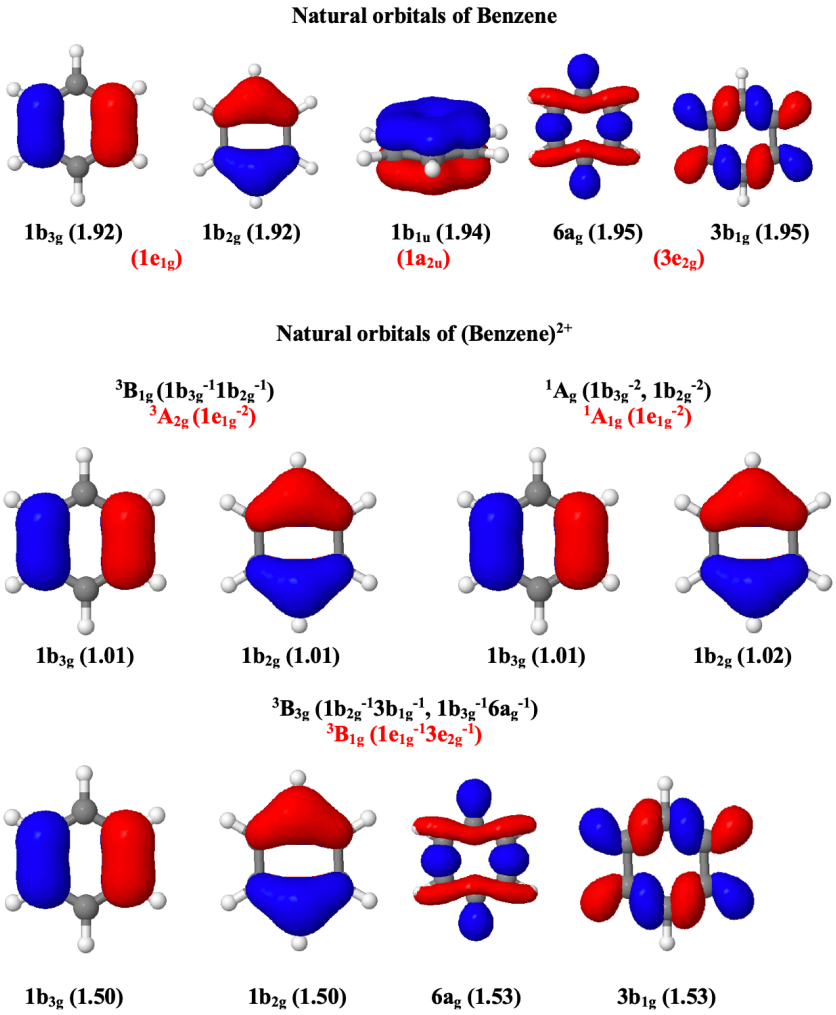

FIG. 5: Frontier NOs and their occupation numbers for the ground state of benzene and selected doubly ionized states. Irreducible representations are given for the D_{6h} point group (in red) and for the largest Abelian subgroup (D_{2h}, in black).

B. Density of states

Fig. 6 shows the densities of singlet and triplet DIP states computed with EOM-DIP-CCSD together with the ADC(2) results from Ref. 55. As discussed in Sec. II A and in Ref. 55, the density of DIP states can be considered as a crude approximation to the Auger spectrum.

Fig. 6 illustrates that, after application of a broadening function, most DIP states are no longer individually discernible. Rather, a spectrum with a few broad peaks, each comprising

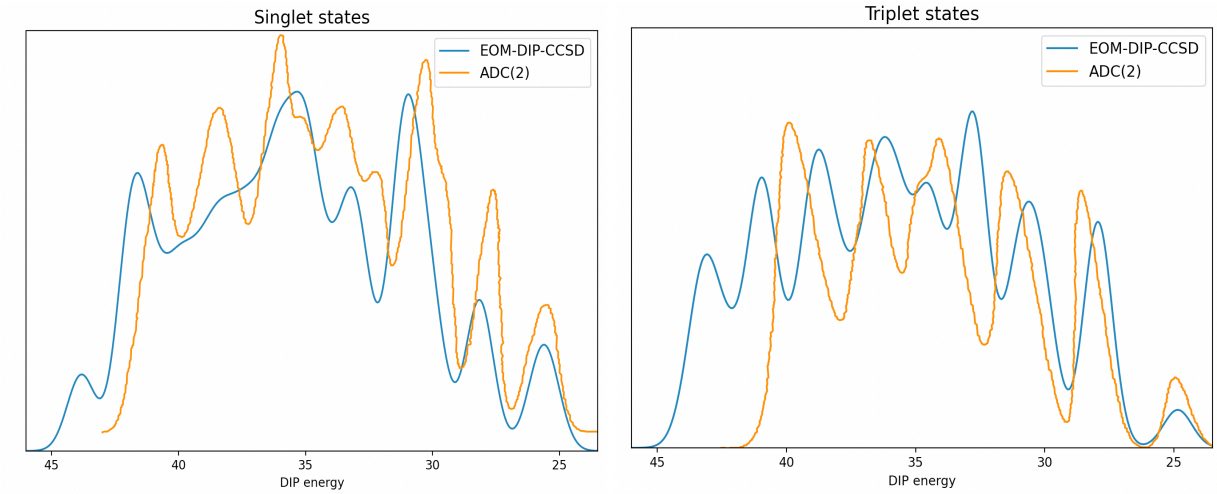

FIG. 6: Density of singlet and triplet DIP states in benzene computed with EOM-DIP-CCSD/u6-311(2+,+)G** and ADC(2) (from Ref. 55). To match the lowest-lying EOM-DIP-CCSD peaks, the ADC(2) data were shifted by 2.15 eV and 1.33 eV for singlet and triplet states, respectively.

many DIP states, is obtained. An exception is the lowest peak in the triplet manifold at 25 eV, which corresponds to the $^3A_{2g}$ state. This state (first entry in Table II) originates from double ionization of the doubly degenerate HOMO. The lowest-lying singlet peak at around 26 eV is composed of two states ($^1E_{2g}$ and $^1A_{1g}$), which are derived by ionization of the HOMO (see Table II). The next two peaks, which are well separated from the higher-lying ones, comprise four triplet and three singlet channels, respectively, as detailed in Table II. Beyond 30 eV, each peak in the singlet and the triplet spectrum comprises even a larger number of DIP states.

Fig. 6 shows that, after application of a uniform shift, the agreement between EOM-DIP-CCSD and ADC(2) is very good for the lowest two peaks in each panel, still acceptable for the third peak, and substantially worse at higher energies. While the uniform shift can be justified by the well-known performance of EOM-CCSD and ADC(2) (see Sec. III A), the reason for deteriorating agreement at higher energies is less obvious. It may be related to the increasing admixture of $3h1p$ configurations that we observe in the higher-lying DIP states. ADC(2) treats these doubly excited configurations at a lower level than EOM-CCSD, which may lead to poor description of states in which the weight of these configurations becomes comparable to the weight of the $2h$ configurations.

Importantly, Fig. 6 only provides a crude picture of the Auger spectrum. The most

important shortcoming is that it suggests equal contributions of singlet and triplet channels to the spectrum, whereas it is clear from theoretical considerations that the contributions of triplet states are smaller (see Appendix). One needs to compute partial widths of the decay channels for quantitative modeling, and we do so in the next section.

C. Total Auger spectrum

The non-resonant Auger spectra of benzene computed with the two different methods discussed in Section II (Feshbach-Fano and CBFs), are shown in Fig. 7. The largest partial widths are given in Tables **??** and **??** in the SI. Notably, there are many channels with partial widths of the same order of magnitude and there is not a single channel with a width of more than 2 meV. Thus, the data in the tables cannot be interpreted without actually constructing the spectrum.

The comparison of the two spectra in Fig. 7 illustrates the very good agreement between the two theoretical approaches, in spite of the vastly different treatment of the outgoing electron. This cross-validates our two approaches. For the CBF method, Fig. **??** in the SI shows how using Eq. (4) instead of Eq. (5) for the peak positions leads to a substantially different Auger spectrum. This demonstrates the importance of using a high-level electronic-structure model.

The two spectra in Fig. 7 have eight and nine distinct peaks, respectively, which we loosely group into the following categories based on the Auger electron energies: a) peaks above 262 eV, b) peaks between 252 and 262 eV, and c) peaks below 252 eV. The two peaks above 262 eV are the easiest to describe. They correspond to the two lowest peaks in the density of singlet states (see Fig. 6) and arise from double ionization of the HOMO and mixed ionization of HOMO/HOMO-1, respectively.

In the range between 252 and 262 eV, each peak is composed of many decay channels. As one would expect, contributions from lower-lying orbitals become more important with decreasing Auger electron energy. We observe that the final states in this energy range have a predominant $2h$ character and are thus well represented by EOM-DIP-CCSD. Below 252 eV, contributions from lower-lying orbitals gain even more weight and the final states develop substantial $3h1p$ character, which makes their description by EOM-DIP-CCSD less reliable. This affects both spectra in Fig. 7 equally.

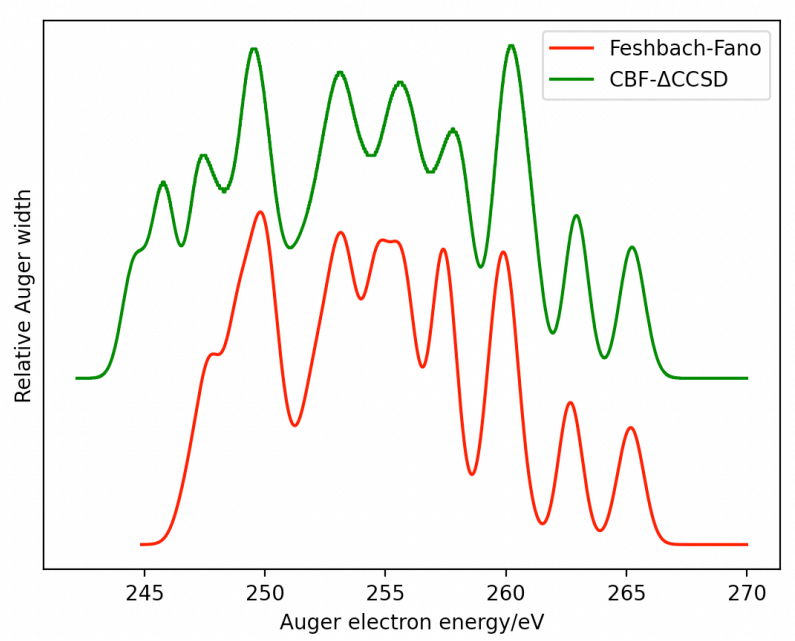

FIG. 7: The non-resonant Auger spectrum of benzene computed using the Feshbach-Fano approach (red curve) and the CBF approach (green curve). The DIP energies needed for the positions of the peaks were computed with EOM-DIP-CCSD for both approaches (see Secs. II B and II C).

Additionally, we investigated the contributions of singlet and triplet states to the computed spectra. As discussed in the Appendix and in Refs. 55 and 82, singlet channels are expected to have notably larger Auger intensities in comparison to triplet channels. Fig. 8 shows that this is indeed the case with both approaches—the Auger spectrum of benzene is dominated by contributions from singlets.

Interestingly, the $^3A_{2g}$ ground state of the benzene dication has zero Auger intensity in

both of our approaches (Feshbach-Fano and CBF). Likewise, the contributions of the low-lying triplets listed in Table II are very small. Only below 260 eV, the triplet contributions become noticeable. At these energies, they visibly affect the shape of the spectrum. This is most evident for the peak around 250 eV, which becomes the most intense peak in the spectrum due to the combined contributions of singlets and triplets. We reiterate that such differences in the Auger intensity of singlet and triplet channels are not apparent from the density of states shown in Fig. 6. Thus, a mere analysis of decay channels does not provide a complete picture of Auger decay.

Furthermore, we note that the triplet contributions are overestimated by the Feshbach-Fano approach as compared to the CBF approach. Such overestimation of triplet intensities was observed in previous studies, where it was attributed to the limitations of the plane-wave treatment of the Auger electron.[75] It was also shown that using Coulomb waves improves the results.[14,75]. Despite this limitation of the plane-wave treatment, the overall spectrum in Fig. 7 is barely affected; Feshbach-Fano and CBF agree well with each other in the entire energy range.

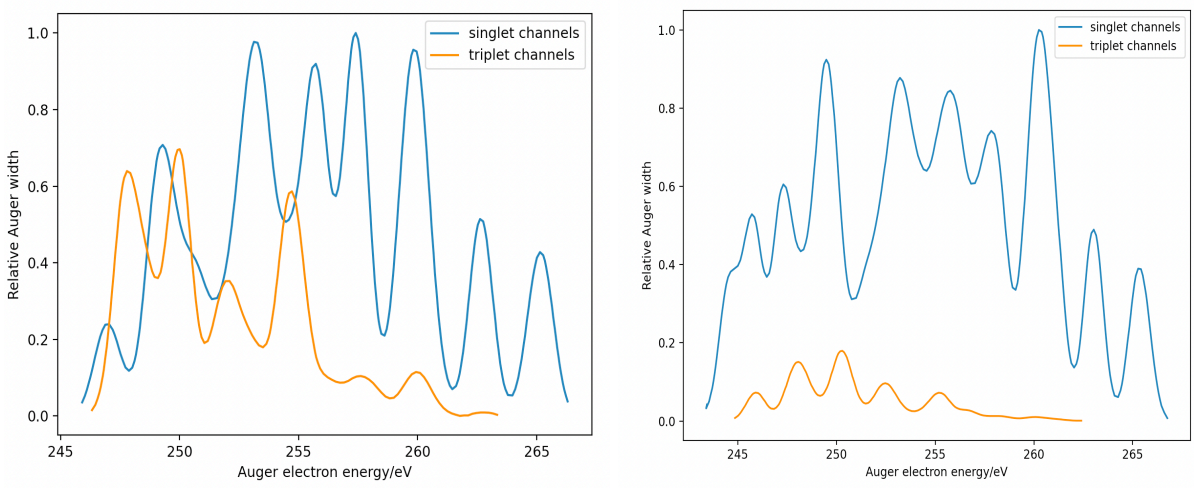

FIG. 8: Contributions from singlet and triplet decay channels to the non-resonant Auger spectrum of benzene. Left: Feshbach-Fano approach, right: CBF approach.

D. Auger spectra corresponding to individual core-ionized states

To analyze the contributions of the four different core-ionized states ($^2A_{1g}$, $^2E_{1u}$, $^2E_{2g}$, $^2B_{1u}$) to the overall Auger spectrum in Fig. 7, we plotted the spectra resulting from selective ionization in Fig. 9. Here, the contributions of degenerate core orbitals (e_{1u}, e_{2g}) were added together. We anticipate that our results will provide useful insights into Auger spectroscopy experiments using narrow-band X-rays, which may lead to selective core-ionization.

Our results show that the symmetry of the core holes impacts the intensity pattern despite their very similar energy. Although the individual spectra have a general structure that is similar to that of the overall spectrum in Fig. 7, the decay width corresponding to a particular Auger electron energy differs. For example, the $^2B_{1u}$ state produces enhanced intensity in the Auger electron energy regime around 250 eV, whereas the $^2A_{1g}$ state mostly stimulates an energy regime closer to 255 eV.

The inspection of Fig. 9 also illustrates more substantial differences between the Feshbach-Fano and the CBF approaches that are not visible in the overall spectrum in Fig. 7. For example, it appears that the CBF approach overestimates the intensity of the decay channels around 260 eV for the degenerate core holes (e_{2g} and e_{1u}). This may be due to the shortcoming of the CBF/CCSD approach discussed in Sec. III A, namely that the degeneracy of the e_{2g} and e_{1u} core orbitals is lifted. Fig. **??** shows the same data as in Fig. 9 but normalized together rather than individually, illustrating the effect of the artificial symmetry breaking on the CBF spectra. In addition, Fig. **??** shows that there is more variation among the individual spectra in the CBF approach than in the Feshbach-Fano approach for the non-degenerate core-hole states as well.

E. Total decay widths

We also calculated the total decay widths of all core-ionized states; the results are shown in Table III. The variation in the width among the core holes does not exceed 15%, which is not surprising given that all states are derived from C($1s$) orbitals. However, the widths computed with CBFs are about a factor of two larger than those computed with the Feshbach-Fano approach. This is most likely due to the latter calculations including only a finite number of decay channels. In contrast, In the CBF approach the total decay width is computed

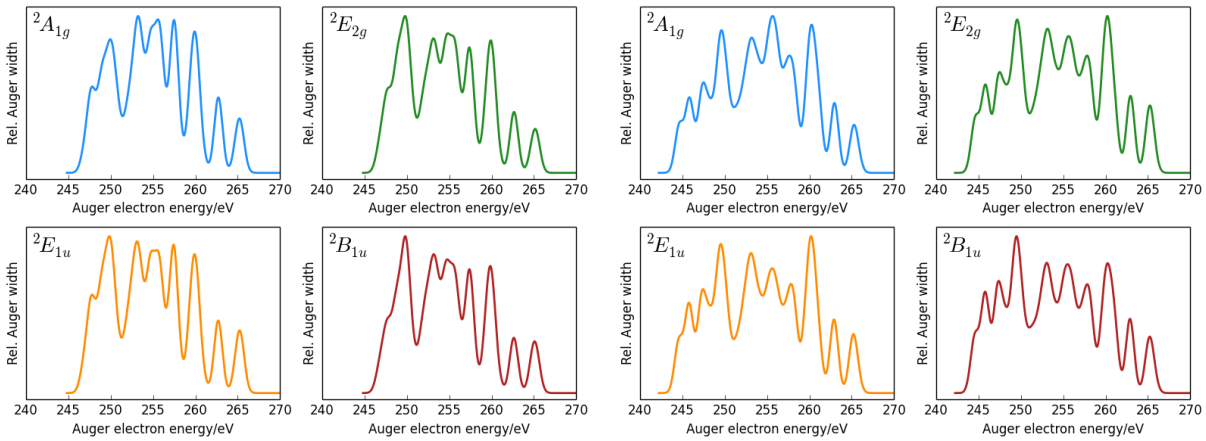

FIG. 9: Auger spectra of benzene corresponding to selective ionization of each core orbital. The spectra are normalized individually and the degenerate core orbitals (e_{1u} and e_{2g}) are treated together. Left: Feshbach-Fano approach. Right: CBF approach.

directly, without considering individual decay channels. We note that both approaches violate symmetry-imposed constraints yielding different widths for degenerate orbitals. In the Feshbach-Fano calculations, the core-hole states are exactly degenerate and the mismatch in widths occurs because a different number of decay channels is included in the calculations. In the CBF approach, the symmetry violation is more pronounced and happens because the core-hole states are described based on independent open-shell CCSD calculations.

TABLE III: Total decay widths of the core-ionized states of benzene in meV.

Core orbital	Feshbach-Fano	CBF
$1a_g$ $(1a_{1g})$	41.70	76.45
$1b_{2u}$ $(1e_{1u})$	44.20	78.84
$1b_{3u}$ $(1e_{1u})$	43.10	84.80
$2a_g$ $(1e_{2g})$	46.20	84.63
$1b_{1g}$ $(1e_{2g})$	47.30	78.02
$2b_{3u}$ $(1b_{1u})$	48.60	75.23
Average width	45.17	79.66

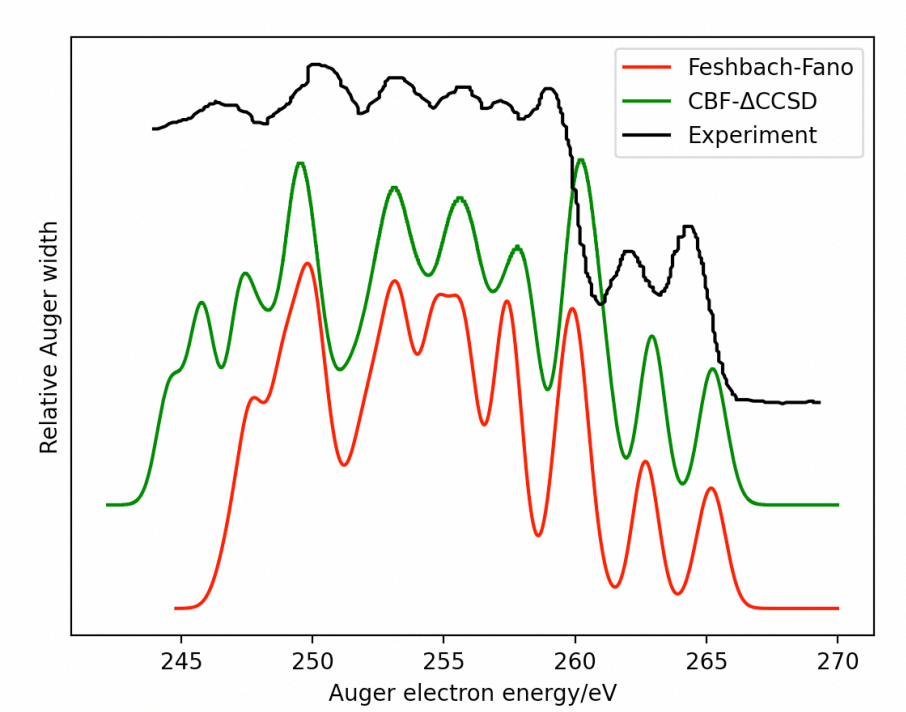

FIG. 10: The theoretical Auger spectra of benzene from Fig. 7 computed using Feshbach-Fano and CBF approaches compared to the most recent experiment.[53] The experimental spectrum is shifted by -1.60 eV to match the theory peak at 253.15 eV.

F. Comparison to the experimental Auger spectrum

Fig. 10 compares the Auger spectrum from the most recent experiment[53] (see Fig. 2, spectrum C) and our theoretical Auger spectra from Fig. 7. The experimental spectrum has a broad structure with various unresolved bands. Eight distinct peaks can be distinguished, two of which are in the high Auger electron energy regime above 262 eV. The latter two peaks, which are relatively well resolved in the experimental spectrum, can be, on the basis of our calculations, unambiguously assigned to final states arising from double ionization of the HOMO and HOMO/HOMO-1, respectively.

However, the intensity pattern of these two peaks differs between theory and experiment. We note that our two theoretical spectra agree with the one reported by Tarantelli *et al.*[55]; on the other hand, the three experimental spectra agree with each other as well in this respect. Provided that the experimental intensity pattern is real and not an artifact of calibration or detection, a possible explanation for the mismatch could be the contribution of resonant Auger decay to the experimental spectra. Both participator and spectator resonant Auger

decay contribute intensity, especially for the higher-energy Auger electrons. The mismatch could also be due to the effect of nuclear motion, which is neglected in the present treatment. For example, it has been demonstrated for the water molecule that vibrational effects can modify Auger intensities considerably.[116] We will explore the intensity mismatch between theory and experiment in future work.

At lower Auger electron energies, the experimental spectrum has five peaks in the region between 250 and 260 eV and one peak below 250 eV. Both theoretical spectra reproduce the intensity pattern of these peaks quite well: (a) all peaks are more intense than the two above 260 eV, (b) the peak below 250 eV is somewhat less intense than the ones between 250 eV and 260 eV, and (c) the most intense peak is the one around 250–251 eV. The weak trend in the intensity between 250 eV and 260 eV is captured better by the Feshbach-Fano approach, whereas the CBF approach seems to overestimate the intensity of the peak at around 260 eV. However, the CBF spectrum is superior below 250 eV, where two well-resolved peaks are obtained, whereas the Feshbach-Fano spectrum only has a weak shoulder (this is likely because we computed fewer DIP states for the latter spectrum).

We also note that the higher electron-energy peaks in the experimental spectrum do not fully align with those in the theoretical spectra even after the experimental spectrum is shifted by 1.60 eV. This misalignment may be either due to an insufficient level of correlation treatment in EOM-IP-CCSD, or due to some problems in the experiments. We reiterate that there is noticeable disagreement between the three measurements, as seen in Fig. 2 and in the SI.

IV. CONCLUSIONS

We have reported a theoretical *ab initio* study of Auger decay in benzene. Partial Auger decay widths were computed with two methods from non-Hermitian quantum chemistry combined with CC and EOM-CC theory. Namely, we used the Feshbach-Fano projection operator approach and, independently, the method of CBFs. In total, we considered over 1,000 transitions corresponding to Auger electron energies in the range from 245 eV to 270 eV, which illustrates the complexity of Auger decay in benzene.

Our two theoretical Auger spectra are in excellent agreement with each other and in reasonable agreement with experimental Auger spectra as well. This showcases the power

of non-Hermitian quantum chemistry and cross-validates the Feshbach-Fano and the CBF approaches. Our Auger spectra are also in qualitative agreement with an Auger spectrum derived from the density of doubly-ionized valence states, which validates the statistical approach of Tarantelli *et al.*[55]

Our work illustrates the strengths and weaknesses of the Feshbach-Fano and the CBF approaches. On the one hand, Feshbach-Fano calculations are computationally less expensive because there is no need for optimizing the complex-scaling angle or complex algebra altogether. Also, smaller basis sets as compared to CBF calculations appear to be sufficient. Moreover, our Feshbach-Fano calculations preserve the degeneracy of the benzene core holes, whereas this is not the case in the CBF treatment, which is based on core-hole reference states. The latter problem could, however, be circumvented by using a closed-shell reference in the CBF calculations.

On the other hand, CBF calculations provide direct access to total decay widths, whereas Feshbach-Fano calculations only yield partial widths. Also, the Feshbach-Fano approach overestimates the contributions of triplet decay channels, likely due to using plane waves for representing the Auger electron, whereas the CBF approach gives more realistic singlet-triplet branching ratios. This shortcoming of the Feshbach-Fano approach can likely be remedied by improving on the plane-wave description.

We note that we could not resolve a conspicuous discrepancy between theory and experiment regarding the intensity of the two peaks in the spectrum with the highest Auger electron energies. This hints at possible extensions of our current work that are worthwhile to pursue: the consideration of resonant contributions to the Auger spectrum as well as the study of vibrational effects.

In conclusion, we see our work as a testament to the power and usefulness of non-Hermitian extensions of *ab initio* quantum-chemical methods. We also expect that our work will serve as a starting point for further theoretical and experimental work in the area of Auger decay.

Appendix A: Auger intensities of singlet versus triplet channels in the Feshbach-Fano approach

Following Ågren and coworkers[81,83], we analyze the expressions of the Auger intensity, Eq. (23), in terms of different spin blocks of the two-body Dyson orbitals to explain differences in relative intensities of triplet and singlet channels. We analyze the contribution to the total intensity due to Γ_r^{pq}; a similar analysis can be carried out for Γ_{pq}^r (left and right Dyson orbitals are slightly different because of the non-Hermitian nature of EOM-CC; for the sake of brevity, only the right part of the transition amplitude is shown in the following equations).

Here, we are interested in the two-electron part of the width, which is computed by contracting the two-body Dyson orbitals[83] Γ_r^{pq}—that connect EOM-IP (Ψ^{N-1}) and EOM-DIP (Ψ^{N-2}) states—with two-electron integrals in which one index corresponds to the plane wave.

From the definition of Γ_r^{pq} [Eq. (21)] and Fig. 4 one can see that index r corresponds to the core orbital and indices p and q — to the valence orbitals. Since the operators for the core and valence orbitals operate in different orbital subspaces, they commute. Therefore, the expression for the two-body Dyson orbital connecting the core-hole state and a DIP state can be written as

$$\Gamma_r^{pq} = \langle \Psi_0 | p^\dagger q^\dagger | \Psi^{N-2} \rangle \tag{27}$$

where Ψ_0 is the neutral CCSD reference state re-created from the EOM-IP state by filling the core hole by operator r. Eq. (27) shows that the leading contribution to Γ is given by the $2h$ DIP amplitudes.

Following these preparations, we can now analyze the spin symmetry of Γ_r^{pq}. First, for a state with an α core-hole, Γ_α^{pq} is non-zero and Γ_β^{pq} is zero; the converse is true for a state with a β hole. For the DIP states with $M_s = 0$, $\Gamma_r^{\alpha\alpha}$ and $\Gamma_r^{\beta\beta} = 0$. By using spin symmetry of the singlet and triplet states with the same orbital occupations, we can write that for a singlet DIP state

$$\Gamma_r^{\alpha\beta} = -\Gamma_r^{\beta\alpha} \tag{28}$$

and for a triplet DIP state

$$\Gamma_r^{\alpha\beta} = \Gamma_r^{\beta\alpha}. \tag{29}$$

To estimate relative contributions to the Auger intensity, we need to carry out spin integration of the two-electron integrals. The expression for the partial width in terms of

different spin blocks can be written as follows, by considering an α core hole and the spin symmetry of $\mathbf{k}$ to be β:

$$\begin{aligned}\widetilde{\Gamma} &= \frac{1}{2}\sum_{pqr}\langle pq||\mathbf{k}r_\alpha\rangle\Gamma_{r_\alpha}^{pq} = \frac{1}{2}\sum_{pqr}\langle p_\alpha q_\beta||\mathbf{k}_\beta r_\alpha\rangle\Gamma_{r_\alpha}^{p_\alpha q_\beta} + \frac{1}{2}\sum_{pqr}\langle p_\beta q_\alpha||\mathbf{k}_\beta r_\alpha\rangle\Gamma_{r_\alpha}^{p_\beta q_\alpha} \\ &= \frac{1}{2}\sum_{pqr}[\langle p_\alpha q_\beta|\mathbf{k}_\beta r_\alpha\rangle - \langle p_\alpha q_\beta|r_\alpha\mathbf{k}_\beta\rangle]\Gamma_{r_\alpha}^{p_\alpha q_\beta} + \frac{1}{2}\sum_{pqr}[\langle p_\beta q_\alpha|\mathbf{k}_\beta r_\alpha\rangle - \langle p_\beta q_\alpha|r_\alpha\mathbf{k}_\beta\rangle]\Gamma_{r_\alpha}^{p_\beta q_\alpha} \\ &= \frac{1}{2}\sum_{pqr}[-\langle p_\alpha q_\beta|r_\alpha\mathbf{k}_\beta\rangle\Gamma_{r_\alpha}^{p_\alpha q_\beta} + \langle p_\beta q_\alpha|\mathbf{k}_\beta r_\alpha\rangle\Gamma_{r_\alpha}^{p_\beta q_\alpha}]\end{aligned} \tag{30}$$

Integrating the spins out and substituting Eq. (29), the partial widths become:

$$\begin{aligned}\widetilde{\Gamma}_{singlet} &= \frac{1}{2}\sum_{pqr}[\langle pq|\mathbf{k}r\rangle + \langle pq|r\mathbf{k}\rangle]\Gamma_r^{pq}, \\ \widetilde{\Gamma}_{triplet} &= \frac{1}{2}\sum_{pqr}[\langle pq|\mathbf{k}r\rangle - \langle pq|r\mathbf{k}\rangle]\Gamma_r^{pq}.\end{aligned} \tag{31}$$

In the above expressions, indices p, q, and r correspond to spatial orbitals. As one can see, in the singlet contribution, the two two-electron integrals, which can be interpreted as Coulomb interaction between the core hole, the valence electrons, and a free electron, are connected by a plus sign, whereas in the triplet contribution they are connected by a minus sign, leading to partial cancellation.

Appendix B: Auger intensities of singlet versus triplet channels in the complex basis function approach

As discussed in Sec. II C, the Auger intensities can be computed from the partial decay widths obtained through energy decomposition analysis of the imaginary part of the CBF-CCSD energy in Eq. (26). For the purpose of this work, the contribution of the singles amplitudes is negligible[76] and is therefore omitted in the following discussion. The partial decay width of a specific channel μ can then be written as

$$-\frac{\Gamma_\mu}{2} = \frac{1}{4}\,\mathrm{Im}\Big[t_{ij}^{ab}\langle ij||ab\rangle + t_{ji}^{ab}\langle ji||ab\rangle + t_{ij}^{ba}\langle ij||ba\rangle + t_{ji}^{ba}\langle ij||ab\rangle\Big] = \mathrm{Im}\Big[t_{ij}^{ab}\langle ij||ab\rangle\Big]\ . \tag{32}$$

where a, b, i, j refer to spin orbitals. We now consider the CBF-CCSD energy of a core-ionized state where the core hole has β spin. Then, if index a refers to the core hole, b represents the outgoing Auger electron and can have α or β spin. i and j are valence

orbitals and can also have either α or β spin. Thus, we end up with three spin cases: $t_{i_\beta j_\beta}^{a_\beta b_\beta}$, $t_{i_\beta j_\alpha}^{a_\beta b_\alpha}$, $t_{i_\alpha j_\beta}^{a_\beta b_\alpha}$.

Recalling that b stands for the outgoing Auger electron, the first spin case can be related to a triplet final state, while the other two spin cases correspond to singlet final states. The contributions to the decay width can thus be written as:

$$-\frac{\Gamma_\mu^{\text{triplet}}}{2} = \text{Im}\Big[t_{i_\beta j_\beta}^{a_\beta b_\beta}\Big(\langle a_\beta b_\beta | i_\beta j_\beta\rangle - \langle a_\beta b_\beta | j_\beta i_\beta\rangle\Big)\Big] \tag{33}$$

$$\begin{aligned}-\frac{\Gamma_\mu^{\text{singlet}}}{2} &= \text{Im}\Big[t_{i_\beta j_\alpha}^{a_\beta b_\alpha}\Big(\langle a_\beta b_\alpha | i_\beta j_\alpha\rangle - \langle a_\beta b_\alpha | j_\alpha i_\beta\rangle\Big) + t_{i_\alpha j_\beta}^{a_\beta b_\alpha}\Big(\langle a_\beta b_\alpha | i_\alpha j_\beta\rangle - \langle a_\beta b_\alpha | j_\beta i_\alpha\rangle\Big)\Big] \\ &= \text{Im}\Big[t_{i_\beta j_\alpha}^{a_\beta b_\alpha}\langle a_\beta b_\alpha | i_\beta j_\alpha\rangle - t_{i_\alpha j_\beta}^{a_\beta b_\alpha}\langle a_\beta b_\alpha | j_\beta i_\alpha\rangle\Big]\end{aligned} \tag{34}$$

Eqs. (33) and (34) represent contributions to the imaginary part of the same-spin and opposite-spin correlation energy. From this, we can already conclude that the partial widths of the triplet channels are smaller than those of the singlet channels because it is well known that the opposite-spin correlation energy is usually considerably higher that the same-spin correlation energy.[117]

If we are in the case of a closed-shell reference $t_{i_\alpha j_\beta}^{a_\beta b_\alpha} = -t_{j_\beta i_\alpha}^{a_\beta b_\alpha} = -t_{i_\beta j_\alpha}^{a_\beta b_\alpha}$, which allows to simplify Eq. (34) further so that we obtain final expressions that are similar to Eq. (31) in Appendix A:

$$-\frac{\Gamma_\mu^{\text{triplet}}}{2} = \text{Im}\Big[t_{ij}^{ab}\Big(\langle ab|ij\rangle - \langle ab|ji\rangle\Big)\Big] \tag{35}$$

$$-\frac{\Gamma_\mu^{\text{singlet}}}{2} = \text{Im}\Big[t_{ij}^{ab}\Big(\langle ab|ij\rangle + \langle ab|ji\rangle\Big)\Big] \tag{36}$$

with a, b, i, j now referring to spatial orbitals.

Acknowledgments

N.K.J. and A. F.-P. contributed equally. This work was supported in Los Angeles by the U.S. National Science Foundation (No. CHE-1856342 to A.I.K.) and in Leuven by the European Research Council (ERC) under the European Union's Horizon 2020 research and innovation program (Grant No. 851766 to T.C.J.), by the Fonds der Chemischen Industrie (Kekulé fellowship K 208/24 to F.M.) and by the Flemish Supercomputer Centrum funded by the Research Foundation–Flanders and the Flemish government.

Conflicts of interest

The authors declare the following competing financial interest(s): A.I.K. is the president and a part-owner of Q-Chem, Inc.

[1] B. K. Agarwal, *X-ray spectroscopy: an introduction*, volume 15. Springer, 2013.

[2] D. Spanjaard, C. Guillot, M.-C. Desjonqueres, G. Tréglia, and J. Lecante, Surface core level spectroscopy of transition metals: A new tool for the determination of their surface structure, Surf. Sci. Rep. **5**, 1 (1985).

[3] M. Tchaplyguine, R. Feifel, R. R. T. Marinho, M. Gisselbrecht, S. L. Sorensen, A. N. de Brito, N. Mårtensson, S. Svensson, and O. Björneholm, Selective probing of the electronic structure of free clusters using resonant core-level spectroscopy, Chem. Phys. **289**, 3 (2003).

[4] M. Nisoli, P. Decleva, F. Calegari, A. Palacios, and F. Martín, Attosecond electron dynamics in molecules, Chem. Rev. **117**, 10760 (2017).

[5] P. M. Kraus, M. Zürch, S. K. Cushing, D. M. Neumark, and S. R. Leone, The ultrafast x-ray spectroscopic revolution in chemical dynamics, Nat. Rev. Chem. **2**, 82 (2018).

[6] B. K. McFarland, J. P. Farrell, S. Miyabe, F. Tarantelli, A. Aguilar, N. Berrah, C. Bostedt, J. D. Bozek, P. H. Bucksbaum, J. C. Castagna, R. N. Coffee, J. P. Cryan, L. Fang, R. Feifel, K. J. Gaffney, J. M. Glownia, T. J. Martinez, M. Mucke, B. Murphy, A. Natan, T. Osipov, V. S. Petrović, S. Schorb, Th. Schultz, L. S. Spector, M. Swiggers, I. Tenney, S. Wang, J. L. White, W. White, and M. Gühr, Ultrafast x-ray Auger probing of photoexcited molecular dynamics, Nat. Comm. **5**, 1 (2014).

[7] K. Ramasesha, S. R. Leone, and D. M. Neumark, Real-time probing of electron dynamics using attosecond time-resolved spectroscopy, Annu. Rev. Phys. Chem. **67**, 41 (2016).

[8] P. Norman and A. Dreuw, Simulating X-ray spectroscopies and calculating core-excited states of molecules, Chem. Rev. **118**, 7208 (2018).

[9] T. Fransson, Y. Harada, N. Kosugi, N. A. Besley, B. Winter, J. J. Rehr, L. G. M. Pettersson, and A. Nilsson, X-ray and electron spectroscopy of water, Chem. Rev. **116**, 7551 (2016).

[10] L. Meitner, About the β ray spectra and their connection with the γ radiation, Z. Phys. **11**, 35 (1922).

[11] P. Auger, Secondary β-rays produced in a gas by X-rays, Comptes Rendus Acad. Sci. Paris **177**, 169 (1923).

[12] T. A. Carlson and M. O. Krause, Experimental evidence for double electron emission in an Auger process, Phys. Rev. Lett. **14**, 390 (1965).

[13] A. Müeller, A. Borovik Jr, T. Buhr, J. Hellhund, K. Holste, A. L. D. Kilcoyne, S. Klumpp, M. Martins, S. Ricz, J. Viefhaus, and S. Schippers, Observation of a four-electron Auger process in near-K-edge photoionization of singly charged carbon ions, Phys. Rev. Lett. **114**, 013002 (2015).

[14] W. Skomorowski and A. I. Krylov, Feshbach-Fano approach for calculation of Auger decay rates using equation-of-motion coupled-cluster wave functions. I. Theory and implementation, J. Chem. Phys. **154**, 08124 (2021).

[15] L. A. Harris, Analysis of materials by electron-excited Auger electrons, J. App. Phys. **39**, 1419 (1968).

[16] R. Weissmann and K. Müller, Auger electron spectroscopy-a local probe for solid surfaces, Surf. Sci. Rep. **1**, 251 (1981).

[17] C. J. Powell and M. P. Seah, Precision, accuracy, and uncertainty in quantitative surface analyses by Auger-electron spectroscopy and x-ray photoelectron spectroscopy, J. Vac. Sci. Technol., A **8**, 735 (1990).

[18] T. Orvis, M. Surendran, Y. Liu, A. Cunniff, and J. Ravichandran, In situ Auger electron spectroscopy of complex oxide surfaces grown by pulsed laser deposition, J. Vac. Sci. Technol., A **37**, 061401 (2019).

[19] Z. Li and U. Becker, Chemical state effects on the Auger transitions in Cr, Fe, and Cu compounds, J. Electron. Spectrosc. and Relat. Phenom. **237**, 146893 (2019).

[20] D. F. Stein, Applications of Auger spectroscopy to materials research, J. Vac. Sci. Technol. **12**, 268 (1975).

[21] S. Hofmann, *Auger-and X-ray photoelectron spectroscopy in materials science: a user-oriented guide*, volume 49. Springer Science & Business Media, 2012.

[22] Z. Azdad, L. Marot, L. Moser, R. Steiner, and E. Meyer, Valence band behaviour of zirconium oxide, photoelectron and Auger spectroscopy study, Sci. Rep. **8**, 1 (2018).

[23] L.-C. Chao and S.-H. Yang, Growth and Auger electron spectroscopy characterization of donut-shaped ZnO nanostructures, Appl. Surf. Sci. **253**, 7162 (2007).

[24] S. N. Raman, D. F. Paul, J. S. Hammond, and K. D. Bomben, Auger electron spectroscopy and its application to nanotechnology, Microscopy today **19**, 12 (2011).

[25] R. R. Rye, T. E. Madey, J. E. Houston, and P. H. Holloway, Chemical-state effects in Auger electron spectroscopy, J. Chem. Phys. **69**, 1504 (1978).

[26] R. R. Rye and J. E. Houston, Molecular auger spectroscopy, Acc. Chem. Res. **17**, 41 (1984).

[27] O. Plekan, H. Sa'adeh, A. Ciavardini, C. Callegari, G. Cautero, C. Dri, M. Di Fraia, K. C. Prince, R. Richter, R. Sergo, L. Stebel, M. Devetta, D. Faccialá, C. Vozzi, L. Avaldi, P. Bolognesi, M. C. Castrovilli, D. Catone, M. Coreno, F. Zuccaro, E. Bernes, G. Fronzoni, and D. Toffoli and A. Ponzi, Experimental and theoretical photoemission study of indole and its derivatives in the gas phase, J. Phys. Chem. A **124**, 4115 (2020).

[28] T. Marchenko, L. Inhester, G. Goldsztejn, O. Travnikova, L. Journel, R. Guillemin, I. Ismail, D. Koulentianos, D. Céolin, R. Püttner, M. N. Piancastelli, and M. Simon, Ultrafast nuclear dynamics in the doubly-core-ionized water molecule observed via Auger spectroscopy, Phys. Rev. A **98**, 063403 (2018).

[29] A. Ku, V. J. Facca, Z. Cai, and R. M. Reilly, Auger electrons for cancer therapy—a review, EJNMMI Radiopharm. Chem. **4**, 1 (2019).

[30] G. Pirovano, S. A. Jannetti, L. M. Carter, A. Sadique, S. Kossatz, N. Guru, P. Demétrio De Souza França, M. Maeda, B. M. Zeglis, J. S. Lewis, J. L. Humm, and T. Reiner, Targeted brain tumor radiotherapy using an Auger emitter, Clin. Cancer Res. **26**, 2871 (2020).

[31] J. Borbinha, P. Vaz, and S. Di Maria, Dosimetric assessment in different tumour phenotypes with Auger electron emitting radionuclides: ^{99m}Tc, ^{125}I, ^{161}Tb, and ^{177}Lu, Radiat. Phys. Chem. **172**, 108763 (2020).

[32] G. Pirovano, T. C. Wilson, and T. Reiner, Auger: The future of precision medicine, Nucl. Med. and Bio. **96**, 50 (2021).

[33] A. I. Kassis, The amazing world of Auger electrons, Int. J. Radiat. Bio. **80**, 789 (2004).

[34] A. I. Kassis and S. J. Adelstein, Radiobiologic principles in radionuclide therapy, J. Nucl. Med. **46**, 4S (2005).

[35] F. Buchegger, F. Perillo-Adamer, Y. M. Dupertuis, and A. Bischof Delaloye, Auger radiation targeted into DNA: a therapy perspective, Eur. J. Nucl. Med. Mol. Imaging **33**, 1352 (2006).

[36] L. S. Cederbaum, W. Domcke, and J. Schirmer, Many-body theory of core holes, Phys. Rev. A **22**, 206 (1980).

[37] L. Karlsson, L. Mattsson, R. Jadrny, T. Bergmark, and K. Siegbahn, Valence electron spectra of benzene and the hexafluorides of sulphur, molybdenum, tungsten and uranium. An application of multichannel detector technique to UV-valence electron spectroscopy, Physica Scripta **14**, 230 (1976).

[38] J. A. Horsley, J. Stöhr, A. P. Hitchcock, D. C. Newbury, A. L. Johnson, and F. Sette, Resonances in the K-shell excitation spectra of benzene and pyridine: Gas phase, solid, and chemisorbed states, J. Chem. Phys. **83**, 6099 (1985).

[39] P. Skytt, J. Guo, N. Wassdahl, J. Nordgren, Y. Luo, and H. Ågren, Probing symmetry breaking upon core excitation with resonant x-ray fluorescence, Phys. Rev. A **52**, 3572 (1995).

[40] E. E. Rennie, C. A. F. Johnson, J. E. Parker, D. M. P. Holland, D. A. Shaw, and M. A. Hayes, A photoabsorption, photodissociation and photoelectron spectroscopy study of C_6H_6 and C_6D_6, Chem. Phys. **229**, 107 (1998).

[41] E. S. Subramaniam Iyer, A. Sadybekov, O. Lioubashevski, A. I. Krylov, and S. Ruhman, Rewriting the story of excimer formation in liquid benzene, J. Phys. Chem. A **121**, 1962 (2017).

[42] M. Epshtein, V. Scutelnic, Z. Yang, T. Xue, M. L. Vidal, Anna I. Krylov, S. Coriani, and S. R. Leone, Table-top X-ray spectroscopy of benzene radical cation, J. Phys. Chem. A **124**, 9524 (2020).

[43] K. D. Nanda, M. L. Vidal, R. Faber, S. Coriani, and A. I. Krylov, How to stay out of trouble in RIXS calculations within the equation-of-motion coupled-cluster damped response theory framework? Safe hitchhiking in the excitation manifold by means of core-valence separation, Phys. Chem. Chem. Phys. **22**, 2629 (2020).

[44] K. D. Nanda, M. L. Vidal, R. Faber, S. Coriani, and A. I. Krylov, Correction: "How to stay out of trouble in RIXS calculations within the equation-of-motion coupled-cluster damped response theory framework? Safe hitchhiking in the excitation manifold by means of core-valence separation", Phys. Chem. Chem. Phys. **22**, 17749 (2020).

[45] M. L. Vidal, M. Epshtein, V. Scutelnic, Z. Yang, T. Xue, S. R. Leone, A. I. Krylov, and S. Coriani, The interplay of open-shell spin-coupling and Jahn-Teller distortion in benzene radical cation probed by x-ray spectroscopy, J. Phys. Chem. A **124**, 9532 (2020).

[46] J. Gauss and J.F. Stanton, The equilibrium structure of benzene, J. Phys. Chem. A **104**, 2865 (2000).

[47] P. A. Pieniazek, S. E. Bradforth, and A. I. Krylov, Charge localization and Jahn-Teller distortions in the benzene dimer cation, J. Chem. Phys. **129**, 074104 (2008).

[48] M. O. Sinnokrot and C. D. Sherrill, High-accuracy quantum mechanical studies of pi-pi interactions in benzene dimers, J. Phys. Chem. A **110**, 10656 (2006).

[49] H. Koppel, M. Doscher, I. Baldea, H.D. Meyer, and P.G. Szalay, Multistate vibronic interactions in the benzene radical cation. II. Quantum dynamical simulations, J. Chem. Phys. **117**, 2657 (2002).

[50] M. Doscher, H. Köppel, and P.G. Szalay, Multistate vibronic interactions in the benzene radical cation. I. Electronic structure calculations, J. Chem. Phys. **117**, 2645 (2002).

[51] R. Spohr, T. Bergmark, N. Magnusson, L.O. Werme, C. Nordling, and K. Siegbahn, Electron spectroscopic investigation of Auger processes in bromine substituted methanes and some hydrocarbons, Phys. Scr. **2**, 31 (1970).

[52] E. E. Rennie, B. Kempgens, H. M. Köppe, U. Hergenhahn, J. Feldhaus, B. S. Itchkawitz, A. L. D. Kilcoyne, A. Kivimäki, K. Maier, M. N. Piancastelli, M. Polcik, A. Rüdel, and A. M. Bradshaw, A comprehensive photoabsorption, photoionization, and shake-up excitation study of the C1s cross section of benzene, J. Chem. Phys. **113**, 7362 (2000).

[53] S. Carniato, P. Selles, A. Ferté, N. Berrah, A. H. Wuosmaa, M. Nakano, Y. Hikosaka, K. Ito, M. Žitnik, K. Bučar, K. Soejima, D. Jnk, D. Cubaynes, J. M. Bizau, L. Andric, M. A. Khalal, J. Palaudoux, P. Lablanquie, and F. Penent, Single photon simultaneous K-shell ionization/excitation in C_6H_6: Experiment and theory, J. Phys. B **53**, 244010 (2020).

[54] F. Tarantelli, A. Sgamellotti, and L. S. Cederbaum, The calculation of molecular Auger spectra, J. Electron. Spectrosc. Relat. Phenom. **68**, 297 (1994).

[55] F. Tarantelli, A. Sgamellotti, L. S. Cederbaum, and J. Schirmer, Theoretical investigation of many dicationic states and the Auger spectrum of benzene, J. Chem. Phys. **86**, 2201 (1987).

[56] L. S. Cederbaum, F. Tarantelli, A. Sgamellotti, and J. Schirmer, Double vacancies in the core of benzene, J. Chem. Phys. **86**, 2168 (1987).

[57] C. Villani and F. Tarantelli, Double ionization of fluorinated benzenes: Hole localization and delocalization effects, J. Chem. Phys. **120**, 1775 (2004).

[58] F. Mertins and J. Schirmer, Algebraic propagator approaches and intermediate-state representations. I. The biorthogonal and unitary coupled-cluster methods, Phys. Rev. A **53**, 2140 (1996).

[59] A. Dreuw and M. Wormit, The algebraic diagrammatic construction scheme for the polarization propagator for the calculation of excited states, WIREs: Comput. Mol. Sci. **5**, 82 (2015).

[60] U. Fano, Configuration interaction on intensities and phase shifts, Phys. Rev. **124**, 1866 (1961).

[61] H. Feshbach, A unified theory of nuclear reactions. 2, Ann. Phys. (N.Y.) **19**, 287 (1962).

[62] P.-O. Löwdin, Studies in perturbation theory. IV. Solution of eigenvalue problem by projection operator formalism, J. Math. Phys. **3**, 969 (1962).

[63] C. W. McCurdy and T. N. Rescigno, Extension of the method of complex basis functions to molecular resonances, Phys. Rev. Lett. **41**, 1364 (1978).

[64] J. Aguilar and J. M. Combes, A class of analytic perturbations for one-body Schrödinger Hamiltonians, Commun. Math. Phys. **22**, 269 (1971).

[65] E. Balslev and J. M. Combes, Spectral properties of many-body Schrödinger operators with dilatation-analytic interactions, Commun. Math. Phys. **22**, 280 (1971).

[66] W. P. Reinhardt, Complex coordinates in the theory of atomic and molecular structure and dynamics, Annu. Rev. Phys. Chem. **33**, 223 (1982).

[67] W. Domcke, Theory of resonance and threshold effects in electron-molecule collisions: The projection-operator approach, Phys. Reports **208**, 97 (1991).

[68] N. Moiseyev, *Non-Hermitian quantum mechanics*. Cambridge University Press, 2011.

[69] T.-C. Jagau, K. B. Bravaya, and A. I. Krylov, Extending quantum chemistry of bound states to electronic resonances, Annu. Rev. Phys. Chem. **68**, 525 (2017).

[70] T.-C. Jagau, Theory of electronic resonances: fundamental aspects and recent advances, Chem. Comm. **58**, 5205 (2022).

[71] R. J. Bartlett and I. Shavitt, *Many-Body Methods in Chemistry and Physics: MBPT and Coupled-Cluster Theory*. Cambridge University Press, 2009.

[72] A. I. Krylov, Equation-of-motion coupled-cluster methods for open-shell and electronically excited species: The hitchhiker's guide to Fock space, Annu. Rev. Phys. Chem. **59**, 433 (2008).

[73] K. Sneskov and O. Christiansen, Excited state coupled cluster methods, WIREs: Comput. Mol. Sci. **2**, 566 (2012).

[74] R. J. Bartlett, Coupled-cluster theory and its equation-of-motion extensions, WIREs: Comput. Mol. Sci. **2**, 126 (2012).

[75] W. Skomorowski and A. I. Krylov, Feshbach-Fano approach for calculation of Auger decay rates using equation-of-motion coupled-cluster wave functions. II. Numerical examples and benchmarks, J. Chem. Phys. **154**, 084125 (2021).

[76] F. Matz and T.-C. Jagau, Molecular Auger decay rates from complex-variable coupled-cluster

theory, J. Chem. Phys. **156**, 114 (2022).

[77] F. Matz and T.-C. Jagau, Channel-specific core-valence projectors for determining partial auger decay widths, Mol. Phys. , e2105270 (2022).

[78] R. S. Mulliken, Report on notation for the spectra of polyatomic molecules, J. Chem. Phys. **23**, 1997 (1955).

[79] Depending on molecular orientation, symmetry labels corresponding to the same orbital or vibrational mode may be different. Q-Chem's standard molecular orientation is different from that of Mulliken[78]. For example, Q-Chem would place water molecule in the xz plane instead of the yz. Consequently, for C_{2v} symmetry, b_1 and b_2 labels are flipped. More details can be found at http://iopenshell.usc.edu/resources/howto/symmetry/. To avoid confusion with different molecular orientations and relabeling the states, here we report the structures and symmetry labels following the Q-Chem's notations.

[80] G. Wentzel, Über strahlungslose Quantensprünge, Z. Physik **43**, 521 (1927).

[81] H. Ågren, A. Cesar, and C.-M. Liegener, Theory of molecullar Auger spectra, Adv. Quantum Chem. **23**, 1 (1992).

[82] H. Ågren, On the interpretation of molecular valence Auger spectra, J. Chem. Phys. **75**, 1267 (1981).

[83] R. Manne and H. Ågren, Auger transition amplitudes from general many-electron wavefunctions, Chem. Phys. **93**, 201 (1985).

[84] H. Siegbahn, L. Asplund, and P. Kelfve, The Auger electron spectrum of water vapour, Chem. Phys. Lett. **35**, 330 (1975).

[85] A. Albiez, M. Thoma, W. Weber, and W. Mehlhorn, $KL-2,3$ ionization in neon by electron impact in the range 1.5–50 keV: cross sections and alignment, Z. Phys. D **16**, 97 (1990).

[86] E. Epifanovsky, A. T. B. Gilbert, X. Feng, J. Lee, Y. Mao, N. Mardirossian, P. Pokhilko, A. F. White, M. P. Coons, A. L. Dempwolff, Z. Gan, D. Hait, P. R. Horn, L. D. Jacobson, I. Kaliman, J. Kussmann, A. W. Lange, K. U. Lao, D. S. Levine, J. Liu, S. C. McKenzie, A. F. Morrison, K. D. Nanda, F. Plasser, D. R. Rehn, M. L. Vidal, Z.-Q. You, Y. Zhu, B. Alam, B. J. Albrecht, A. Aldossary, E. Alguire, J. H. Andersen, V. Athavale, D. Barton, K. Begam, A. Behn, N. Bellonzi, Y. A. Bernard, E. J. Berquist, H. G. A. Burton, A. Carreras, K. Carter-Fenk, R. Chakraborty, A. D. Chien, K. D. Closser, V. Cofer-Shabica, S. Dasgupta, M. de Wergifosse, J. Deng, M. Diedenhofen, H. Do, S. Ehlert, P.-T. Fang, S. Fatehi, Q. Feng,

T. Friedhoff, J. Gayvert, Q. Ge, G. Gidofalvi, M. Goldey, J. Gomes, C. E. González-Espinoza, S. Gulania, A. O. Gunina, M. W. D. Hanson-Heine, P. H. P. Harbach, A. Hauser, M. F. Herbst, M. Hernández Vera, M. Hodecker, Z. C. Holden, S. Houck, X. Huang, K. Hui, B. C. Huynh, M. Ivanov, Á. Jász, H. Ji, H. Jiang, B. Kaduk, S. Kähler, K. Khistyaev, J. Kim, G. Kis, P. Klunzinger, Z. Koczor-Benda, J. H. Koh, D. Kosenkov, L. Koulias, T. Kowalczyk, C. M. Krauter, K. Kue, A. Kunitsa, T. Kus, I. Ladjánszki, A. Landau, K. V. Lawler, D. Lefrancois, S. Lehtola, R. R. Li, Y.-P. Li, J. Liang, M. Liebenthal, H.-H. Lin, Y.-S. Lin, F. Liu, K.-Y. Liu, M. Loipersberger, A. Luenser, A. Manjanath, P. Manohar, E. Mansoor, S. F. Manzer, S.-P. Mao, A. V. Marenich, T. Markovich, S. Mason, S. A. Maurer, P. F. McLaughlin, M. F. S. J. Menger, J.-M. Mewes, S. A. Mewes, P. Morgante, J. W. Mullinax, K. J. Oosterbaan, G. Paran, A. C. Paul, S. K. Paul, F. Pavošević, Z. Pei, S. Prager, E. I. Proynov, Á. Rák, E. Ramos-Cordoba, B. Rana, A. E. Rask, A. Rettig, R. M. Richard, F. Rob, E. Rossomme, T. Scheele, M. Scheurer, M. Schneider, N. Sergueev, S. M. Sharada, W. Skomorowski, D. W. Small, C. J. Stein, Y.-C. Su, E. J. Sundstrom, Z. Tao, J. Thirman, G. J. Tornai, T. Tsuchimochi, N. M. Tubman, S. P. Veccham, O. Vydrov, J. Wenzel, J. Witte, A. Yamada, K. Yao, S. Yeganeh, S. R. Yost, A. Zech, I. Y. Zhang, X. Zhang, Y. Zhang, D. Zuev, A. Aspuru-Guzik, A. T. Bell, N. A. Besley, K. B. Bravaya, B. R. Brooks, D. Casanova, J.-D. Chai, S. Coriani, C. J. Cramer, G. Cserey, A. E. DePrince, R. A. DiStasio, A. Dreuw, B. D. Dunietz, T. R. Furlani, W. A. Goddard, S. Hammes-Schiffer, T. Head-Gordon, W. J. Hehre, C.-P. Hsu, T.-C. Jagau, Y. Jung, A. Klamt, J. Kong, D. S. Lambrecht, W. Liang, N. J. Mayhall, C. W. McCurdy, J. B. Neaton, C. Ochsenfeld, J. A. Parkhill, R. Peverati, V. A. Rassolov, Y. Shao, L. V. Slipchenko, T. Stauch, R. P. Steele, J. E. Subotnik, A. J. W. Thom, A. Tkatchenko, D. G. Truhlar, T. Van Voorhis, T. A. Wesolowski, K. B. Whaley, H. L. Woodcock, P. M. Zimmerman, S. Faraji, P. M. W. Gill, M. Head-Gordon, J. M. Herbert, and A. I. Krylov, Software for the frontiers of quantum chemistry: An overview of developments in the Q-Chem 5 package, J. Chem. Phys. **155**, 084801 (2021).

[87] A. I. Krylov and P. M. W. Gill, Q-Chem: An engine for innovation, WIREs: Comput. Mol. Sci. **3**, 317 (2013).

[88] J. F. Stanton and R. J. Bartlett, The equation of motion coupled-cluster method. A systematic biorthogonal approach to molecular excitation energies, transition probabilities, and excited state properties, J. Chem. Phys. **98**, 7029 (1993).

[89] S. Coriani and H. Koch, Communication: X-ray absorption spectra and core-ionization potentials within a core-valence separated coupled cluster framework, J. Chem. Phys. **143**, 181103 (2015).

[90] S. Coriani and H. Koch, Erratum: "Communication: X-ray absorption spectra and core-ionization potentials within a core-valence separated coupled cluster framework" [J. Chem. Phys. 143, 181103 (2015)], J. Chem. Phys. **145**, 149901 (2016).

[91] M. L. Vidal, X. Feng, E. Epifanovski, A. I. Krylov, and S. Coriani, A new and efficient equation-of-motion coupled-cluster framework for core-excited and core-ionized states, J. Chem. Theory Comput. **15**, 3117 (2019).

[92] M. L. Vidal, A. I. Krylov, and S. Coriani, Dyson orbitals within the fc-CVS-EOM-CCSD framework: theory and application to X-ray photoelectron spectroscopy of ground and excited states, Phys. Chem. Chem. Phys. **22**, 2693 (2020).

[93] R. Faber and S. Coriani, Resonant inelastic X-ray scattering and nonesonant X-ray emission spectra from coupled-cluster (damped) response theory, J. Chem. Theory Comput. **15**, 520 (2019).

[94] R. Faber and S. Coriani, Core–valence-separated coupled-cluster-singles-and-doubles complex-polarization-propagator approach to X-ray spectroscopies, Phys. Chem. Chem. Phys. **22**, 2642 (2020).

[95] K. D. Nanda and A. I. Krylov, A simple molecular orbital picture of RIXS distilled from many-body damped response theory, J. Chem. Phys. **152**, 244118 (2020).

[96] K. D. Nanda and A. I. Krylov, Cherry-picking resolvents: A general strategy for convergent coupled-cluster damped response calculations of core-level spectra, J. Chem. Phys. **153**, 141104 (2020).

[97] M. L. Vidal, P. Pokhilko, A. I. Krylov, and S. Coriani, Equation-of-motion coupled-cluster theory to model L-edge x-ray absorption and photoelectron spectra, J. Phys. Chem. Lett. **11**, 8314 (2020).

[98] K. W. Sattelmeyer, H. F. Schaefer, and J. F. Stanton, Use of 2h and 3h-p like coupled-cluster Tamm-Dancoff approaches for the equilibrium properties of ozone, Chem. Phys. Lett. **378**, 42 (2003).

[99] J. Shen and P. Piecuch, Doubly electron-attached and doubly ionized equation-of-motion coupled-cluster methods with 4-particle-2-hole and 4-hole-2-particle excitations and their

active-space extensions, J. Chem. Phys. **138**, 194102 (2013).

[100] D. Bokhan, D. N. Trubnikov, A. Perera, and R. J. Bartlett, Explicitly-correlated double ionization potentials and double electron attachment equation-of-motion coupled cluster methods, Chem. Phys. Lett. **692**, 191 (2018).

[101] R. Sarangi, M. L. Vidal, S. Coriani, and A. I. Krylov, On the basis set selection for calculations of core-level states: Different strategies to balance cost and accuracy, Mol. Phys. **118**, e1769872 (2020).

[102] A. I. Krylov, From orbitals to observables and back, J. Chem. Phys. **153**, 080901 (2020).

[103] P.-O. Löwdin, Quantum theory of many-particle systems. I. Physical interpretations by means of density matrices, natural spin-orbitals, and convergence problems in the method of configurational interaction, Phys. Rev. **97**, 1474 (1955).

[104] A. T. B. Gilbert, N. A. Besley, and P. M. W. Gill, Self-consistent field calculations of excited states using the maximum overlap method (MOM), J. Phys. Chem. A **112**, 13164 (2008).

[105] N. A. Besley, A. T. B. Gilbert, and P. M. W. Gill, Self-consistent-field calculations of core excited states, J. Chem. Phys. **130**, 124308 (2009).

[106] T. N. Rescigno, A. E. Orel, and C. W. McCurdy, Application of complex coordinate SCF techniques to a molecular shape resonance: The $^2\Pi_g$ state of N_2^-, J. Chem. Phys. **73**, 6347 (1980).

[107] C. W. McCurdy, T. N. Rescigno, E. R. Davidson, and J. G. Lauderdale, Applicability of self-consistent field techniques based on the complex coordinate method to metastable electronic states, J. Chem. Phys. **73**, 3268 (1980).

[108] B. Simon, The definition of molecular resonance curves by the method of exterior complex scaling, Phys. Lett. **71A** (1979).

[109] N. Moiseyev and J. O. Hirschfelder, Representation of several complex coordinate methods by similarity transformation operators, J. Chem. Phys. **88**, 1063 (1988).

[110] N. Moiseyev, P. R. Certain, and F. Weinhold, Resonance properties of complex-rotated Hamiltonians, Mol. Phys. **36**, 1613 (1978).

[111] A. F. White, E. Epifanovsky, C. W. McCurdy, and M. Head-Gordon, Second order Møller-Plesset and coupled cluster singles and doubles methods with complex basis functions for resonances in electron-molecule scattering, J. Chem. Phys. **146**, 234107 (2017).

[112] T.-C. Jagau, Coupled-cluster treatment of molecular strong-field ionization, J. Chem. Phys.

148, 204102 (2018).

[113] A. F. White, M. Head-Gordon, and C. W. McCurdy, Complex basis functions revisited: Implementation with applications to carbon tetrafluoride and aromatic N-containing heterocycles within the static-exchange approximation, J. Chem. Phys. **142**, 054103 (2015).

[114] M. Hernández Vera and T.-C. Jagau, Resolution-of-the-identity second-order Møller-Plesset perturbation theory with complex basis functions: Benchmark calculations and applications to strong-field ionization of polyacenes, J. Chem. Phys. **152**, 174103 (2020).

[115] J. H. D. Eland, Spectra of the dications of benzene, naphthalene and azulene, Chem. Phys. **345**, 82 (2008).

[116] L. Inhester, C. F. Burmeister, G. Groenhof, and H. Grubmueller, Auger spectrum of a water molecule after single and double core ionization, J. Chem. Phys. **136**, 144304 (2012).

[117] S. Grimme, L. Goerigk, and R. F. Fink, Spin-component-scaled electron correlation methods, WIREs: Comput. Mol. Sci. **2**, 886 (2012).